Nanoscale

REVIEW

View Article Online
View Journal | View Issue

Cite this: *Nanoscale*, 2016, **8**, 8443

Recent advances in nanostructured Nb-based oxides for electrochemical energy storage

Litao Yan,[a,b] Xianhong Rui,[c] Gen Chen,[b] Weichuan Xu,[b] Guifu Zou*[a] and Hongmei Luo*[b]

Received 16th February 2016,
Accepted 30th March 2016

DOI: 10.1039/c6nr01340f

www.rsc.org/nanoscale

For the past five years, nanostructured niobium-based oxides have emerged as one of the most prominent materials for batteries, supercapacitors, and fuel cell technologies, for instance, $TiNb_2O_7$ as an anode for lithium-ion batteries (LIBs), Nb_2O_5 as an electrode for supercapacitors (SCs), and niobium-based oxides as chemically stable electrochemical supports for fuel cells. Their high potential window can prevent the formation of lithium dendrites, and their rich redox chemistry (Nb^{5+}/Nb^{4+}, Nb^{4+}/Nb^{3+}) makes them very promising electrode materials. Their unique chemical stability under acid conditions is favorable for practical fuel-cell operation. In this review, we summarized recent progress made concerning the use of niobium-based oxides as electrodes for batteries (LIBs, sodium-ion batteries (SIBs), and vanadium redox flow batteries (VRBs)), SCs, and fuel cell applications. Moreover, crystal structures, charge storage mechanisms in different crystal structures, and electrochemical performances in terms of the specific capacitance/capacity, rate capability, and cycling stability of niobium-based oxides are discussed. Insights into the future research and development of niobium-based oxide compounds for next-generation electrochemical devices are also presented. We believe that this review will be beneficial for research scientists and graduate students who are searching for promising electrode materials for batteries, SCs, and fuel cells.

[a]*College of Physics, Optoelectronics and Energy & Collaborative Innovation Center of Suzhou Nano Science and Technology, Soochow University, Suzhou 215000, P. R. China. E-mail: zouguifu@suda.edu.cn; Fax: +86-512-65228130; Tel: +86-512-65228130*

[b]*Department of Chemical and Materials Engineering, New Mexico State University, New Mexico 88003, USA. E-mail: hluo@nmsu.edu; Fax: +1 575-646-7706; Tel: +1 575-646-4204*

[c]*School of Energy and Environment, Anhui University of Technology, Maanshan 243002, P. R. China*

1. Introduction

The emission of carbon dioxide and other global warming gases generated from the continuous combustion of fossil fuels, such as coal, gasoline, and natural gas, has led to various environmental issues. In order to reduce the dependence on these finite and non-renewable resources, battery and fuel cell technologies are considered to be clean and

Litao Yan

Litao Yan is currently a Ph.D. candidate in Materials Science and Engineering at New Mexico State University with a research interest in lithium ion batteries and fuel cells. He received his B. S. degree in Materials Physics from Lanzhou University in 2007 and M.S. in Materials Science from the University of Science and Technology of China in 2010. He is co-supervised by Soochow University.

Xianhong Rui

Xianhong Rui received his Ph.D. degree in Materials Science and Engineering from Nanyang Technological University in 2014. Currently he is a professor at the School of Energy and Environment at Anhui University of Technology, China. His research interests include the development of new synthesis methods and nanostructured materials for energy storage devices.

effective strategies, which can realize the concept of zero-emission. Fuel cells, supercapacitors, and batteries are all electrochemical storage devices and share many similarities in that they provide electricity by an electrochemical reaction between two electrodes. A battery stores chemical reactants, such as lithium, sodium, manganese, aluminum, and zinc. Once the energy has been exhausted, the battery must be recharged or disposed of. Fuel cells are different from batteries in that they generate electricity through reactants (hydrogen and oxygen) that are stored externally, so they can produce electricity continuously as long as the reactants continue to be supplied. In short, a fuel-cell vehicle is refueled while a battery-powered vehicle is recharged. Batteries and supercapacitors could be suitable for averaging out energy production from many renewable resources, such as solar, hydropower, geothermal, and wind energy, filling energy shortfalls during on-peak periods.[1–3] Fuel cells have various advantages, such as zero-emission of natural gas (water is the byproduct) and stable power-source generation, (no "memory effect" when they are refueled).[4–6] Therefore, as a promising energy and environmental solution for the future, battery and fuel cell technologies have attracted much attention in materials science and engineering. Commercial vehicles with power sources, such as batteries (Tesla) and fuel cells (Toyota), represent two areas in which significant progress has been achieved. However, we still need to find suitable electrode materials to meet the requirements for high cycle durability, high performance, and low cost.

Recently, niobium-based oxides have emerged as the most prominent materials for batteries, supercapacitors, and fuel cell technologies.[7–9] Their unique chemical stability under acid conditions (niobium-based oxides were applied as highly stable electrochemical supports for fuel cells),[10,11] and their high potential window, which can prevent the formation of lithium dendrites, as well as their rich redox chemistry (Nb^{5+}/Nb^{4+}, Nb^{4+}/Nb^{3+}), which contributes to their high specific capacity/capacitance (higher than those of a conventional $Li_4Ti_5O_{12}$ anode),[12–14] make them very promising electrode materials. Unfortunately, the sluggish lithium-ion diffusivity in niobium-based oxides limits their rate performance. The poor electronic conductivity of Nb_2O_5 reduces the charge transfer in fuel cells and batteries, and the low surface area resulting from a high preparation temperature limits their capacitive contribution. To solve these problems, tremendous research efforts have been made to improve electron transfer and lithium ion diffusion by combining conductive materials (*i.e.* graphene, carbon-coatings, and carbon nanotubes) or reducing the electrode materials to the nanoscale.[15–17] Combining conductive materials with niobium-based oxides and reducing electrode materials to the nanoscale can offer several advantages, including: (i) short path lengths for lithium ion diffusion and electron transport and fast charge transfer, resulting in a fast diffusion rate (*i.e.*, higher power); (ii) increased contact area per unit mass in the electrolyte/electrode, which could enhance the kinetics of lithium-ion diffusion across the interface for batteries (*i.e.*, higher charge/discharge rates) and more ion adsorption sites on the surface or near the surface for charge transfer reactions of supercapacitors (*i.e.*, higher specific capacitances); (iii) a larger surface area to support the noble metal, so as to increase the performance in fuel cells; and (iv) significantly enhanced synergistic effect between the noble metal and metal oxide supports.

Recently, nanostructured TiO_2 and layered transition-metal dichalcogenides for the application of energy storage have been reviewed.[18,19] In this review, we summarize the recent progress made towards niobium-based oxide electrode engineering strategies for batteries, supercapacitors, and fuel cell applications. The crystal structures of niobium-based oxides, especially Nb_2O_5 and $TiNb_2O_7$, are presented. Moreover, charge storage mechanisms, electrochemical performances,

Gen Chen

Gen Chen is currently a Ph.D. candidate in Chemical and Materials Engineering at New Mexico State University with a research interest in the nanoscale engineering of heterostructured composites for energy conversion and storage. He received his B.S. (2009) and M.S. (2012) in Materials Science from the Central South University, China. He joined Los Alamos National Lab. as a visiting researcher (2014–2015). In 2015, he was selected as award winner of the ECS Edward G. Weston Summer Fellowship and Chinese Government Award for Outstanding Self-Financed Students Abroad from the China Scholarship Council.

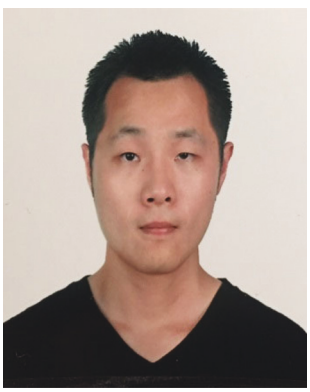

Weichuan Xu

Weichuan Xu is a Ph.D. student in Chemical and Materials Engineering at New Mexico State University with a research interest in the oxygen reduction reaction and the ethanol oxidation reaction. He received his B.S. degree in Chemical Engineering from East China University of Science and Technology in 2014.

cycling stability, and the rate capability of niobium-based oxides are discussed. In addition, insights into the future research and development of niobium-based oxide compounds for next-generation batteries, supercapacitors, and fuel cell devices are provided.

2. Nb-based oxides for LIBs

LIBs play a vital role in our daily lives as the dominant power sources for portable electronics, as well as automotive systems, due to their high energy density, long cycling life, and good environmental compatibility.[20–22] A typical LIB device consists of a positive electrode (anode, *e.g.*, graphite), a lithium-ion conducting electrolyte, and a negative electrode (cathode, *e.g.*, $LiCoO_2$). Upon charging, Li-ions are extracted from the cathode host, pass through the electrolyte, and intercalate into the anode. Discharge is the reverse process. Although such batteries are commercially successful, they cannot fulfill the performance requirements of next-generation LIBs. Further breakthroughs in electrode materials are expected. The demonstration of reversible lithium insertion into transition-metal–oxide anodes has made the advent of high-energy LIBs possible. Among these, lithium titanate ($Li_4Ti_5O_{12}$) and niobium-based oxides have received great interest due to their considerable safety advantages. Their redox potentials (1.0–2.0 V) match with the lowest unoccupied molecular orbital (LUMO) of the organic liquid-carbonate electrolytes, avoiding the formation of a passivating solid-electrolyte-interface (SEI) layer.[23–25] Compared with the low capacity of $Li_4Ti_5O_{12}$ (140 mA h g^{-1}), the high capacity of Nb-based oxides (~200 mA h g^{-1}), which are related to the multiple valences of Nb, could be of great benefit for LIB anodes.[23]

2.1 Niobium oxides

Niobium–oxides mainly exist in the forms of stoichiometric Nb_2O_5 (+5), NbO_2 (+4), Nb_2O_3 (+3), and NbO (+2). Nb_2O_5, an n-type transition metal oxide semiconductor with a band gap of about 3.4 eV, has shown remarkable properties in the fields of gas sensing, catalysis, electrochromics, and photoelectrodes, as well as in LIB anodes.[26–31] Nb_2O_5 exists in many polymorphic forms, *e.g.*, pseudohexagonal (H-Nb_2O_5), orthorhombic (O-Nb_2O_5), tetragonal (T-Nb_2O_5), and monoclinic phases (M-Nb_2O_5).[31–33] Their crystal structures are shown in Fig. 1.[33] M-Nb_2O_5 is the most thermodynamically stable phase, while H-Nb_2O_5 is the least stable one and can be readily transformed into M-Nb_2O_5 by appropriate heat treatment. As shown in the bottom panel of Fig. 1, amorphous Nb_2O_5 synthesized at low temperatures crystallizes into H-Nb_2O_5 or O-Nb_2O_5 at around 500 °C, and transforms to T-Nb_2O_5 at ~800 °C. M-Nb_2O_5 is always produced when heated to temperatures above 1000 °C. Since early studies in the 1980s,[34] considerable effort has been devoted to developing high-performance Nb_2O_5 anodes for LIB applications.

In 1999, Kumagai *et al.*[35] produced H-, O- and M-Nb_2O_5 compounds that formed under different heating temperatures. They displayed high initial discharge capacities of 180–200 mA h g^{-1} with charge–discharge cycling at a potential around 1.5 V *vs.* Li/Li^+ (Fig. 2a–c). The electrochemical reaction was represented as $Nb_2O_5 + xLi^+ + xe^- \leftrightarrow Li_xNb_2O_5$ ($0 \le x \le 2$), but their structural changes were different as a result of electrochemical lithium intercalation. The H- and O-Nb_2O_5 exhibited a single phase $Li_xNb_2O_5$ on discharge, while M-Nb_2O_5 showed a larger repulsive interaction between ions, resulting in a two-phase equilibrium from $x = 1$ to 2 in $Li_xNb_2O_5$. In 2006, the same group[36] examined the electrochemical charge–discharge behavior of Nb_2O_5 phases formed at different temperatures in the range 400–1100 °C by using *in situ* synchrotron radiation (SR), X-ray diffraction (XRD), and *in situ* X-ray absorption fine structure (XAFS) techniques. The electrochemical measurement of Nb_2O_5 phases with various crystals showed that O- and T-Nb_2O_5 had a better cycle life performance in the voltage window 1.2–3.0 V (*vs.* Li/Li^+). The *in situ* SR-XRD patterns indicated that the original crystal structures of O- and T-Nb_2O_5 are

Guifu Zou

Guifu Zou received his Ph.D. degree in Inorganic Chemistry from the University of Science and Technology of China in 2006. Following a postdoctoral position at Umea University, Sweden, he was appointed as a Director's Postdoctoral Fellow at Los Alamos National Lab. from 2007–2011, and he joined Soochow University, China as a Professor in Fall 2011. Currently, his group's research focuses on the growth and integration of thin films and nanostructures for energy storage and conversion.

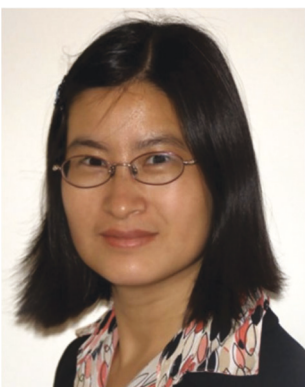

Hongmei Luo

Hongmei Luo received her Ph.D. degree in Chemical Engineering from Tulane University in 2006. She was a postdoctoral research associate at Los Alamos National Lab. from 2006–2009 and she joined the Chemical and Materials Engineering Department at New Mexico State University in Fall 2009. She was promoted to Associate Professor in 2014. Dr Luo's group's research focuses on epitaxial thin films for magnetic and superconducting properties, and nanostructured materials for energy conversion and storage.

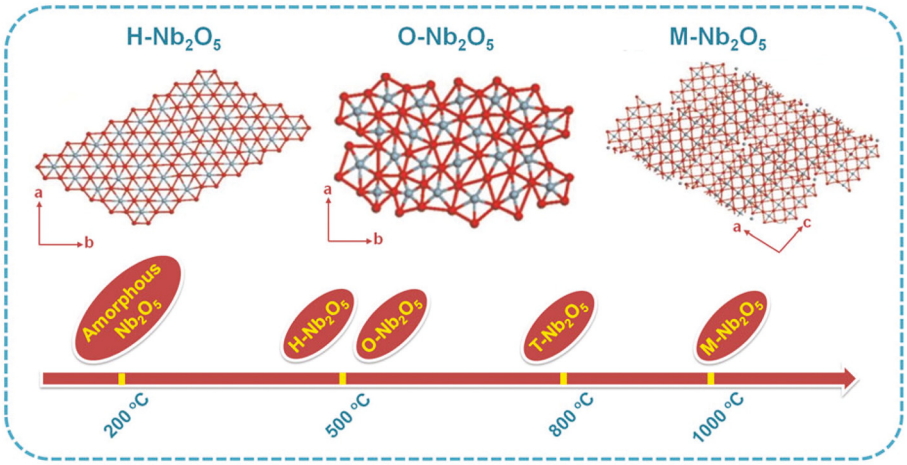

Fig. 1 Structural schemes of H-Nb_2O_5, O-Nb_2O_5, and M-Nb_2O_5, and the evolution of the Nb_2O_5 crystal phase as a function of temperature. Adapted and reproduced, with permission, from ref. 33. Copyright 2012, Co-Action Publishing.

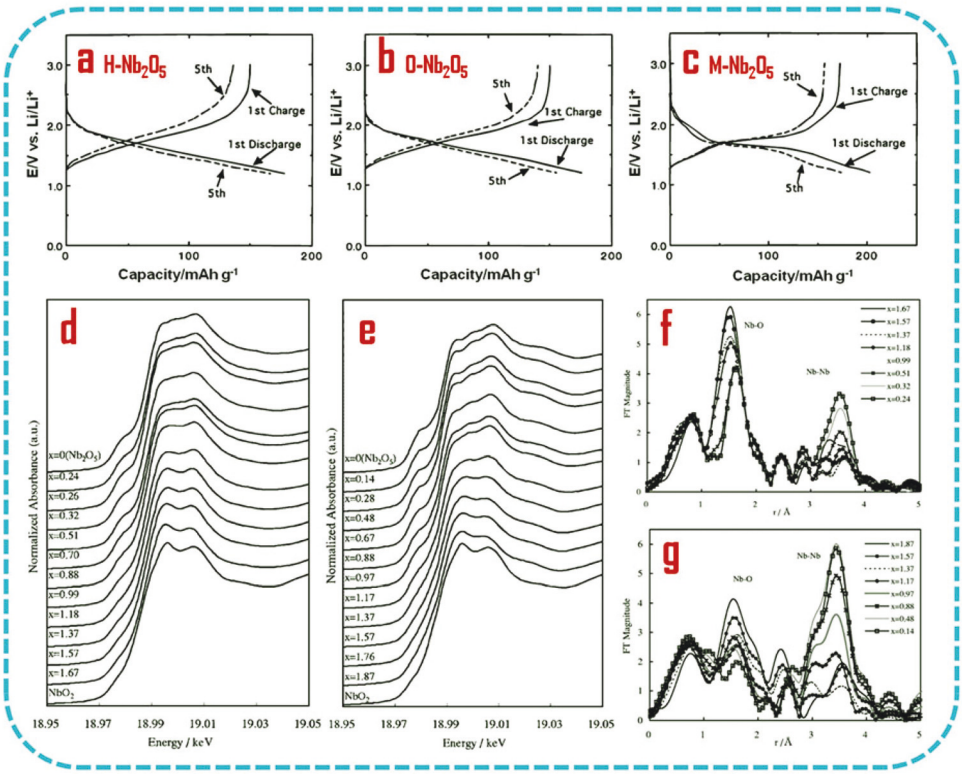

Fig. 2 (a–c) Discharge–charge curves of H-, O- and M-Nb_2O_5 at a current density of 0.1 mA cm^{-2}. Adapted and reproduced, with permission, from ref. 35. Copyright 1999, the Electrochemical Society. (d and e) *In situ* Nb K-edge XANES spectra of O-$Li_xNb_2O_5$ (d) and T-$Li_xNb_2O_5$ (e). (f and g) Radial structure function of O-$Li_xNb_2O_5$ (f) and T-$Li_xNb_2O_5$ (g) obtained by Fourier transforms of the Nb K-edge EXAFS oscillations. Adapted and reproduced, with permission, from ref. 36. Copyright 2006, the Electrochemical Society.

maintained without the appearance of any new phases during the insertion of lithium into their matrices, and their volume change is less than 1%, which guarantees a good battery performance. The *in situ* extended XAFS (EXAFS) spectra of the Nb K-edge in O- and T-$Li_xNb_2O_5$ ($0 \leq x \leq 2$) were further measured. As seen from the Nb K-edge X-ray absorption near-edge structure (XANES) spectra (Fig. 2d and e), the absorption edge shifted continuously to a low-energy side from that of Nb_2O_5 to one similar to that of NbO_2, as the x-value in $Li_xNb_2O_5$ increased, indicating a reduction from Nb^{5+} to Nb^{4+} in both Nb_2O_5 phases. Fig. 2f and g show the Fourier transforms (FTs) of the k^3-weighted Nb K-edge EXAFS oscillations of

$Li_xNb_2O_5$. The first peak at ~1.5 Å is related to the Nb–O interaction in the first coordination sphere, and the second one at ~3.5 Å is ascribed to the Nb–Nb interaction in the second coordination sphere. The Nb–O peak intensity in O-$Li_xNb_2O_5$ is higher than that of the Nb–Nb peak, whereas in T-$Li_xNb_2O_5$, the Nb–Nb peak intensity is much higher than that of the Nb–O peak, due to the two-dimensional (2D) planar arrangement of the Nb atoms in the tetragonal phase. On the other hand, it is found that the intensity decrease of the Nb–Nb peak in the O-type structure is much less than that in the T-type, which is probably associated with lithium intercalation into the vacant interstitial sites in the three-dimensional (3D) framework structure of O-Nb_2O_5. It appeared that the 2D layer structure of T-Nb_2O_5 is more favorable for reversible Li intercalation compared with the 3D structure of O-Nb_2O_5, resulting in a relatively better performance for T-Nb_2O_5. Further progress with respect to Nb_2O_5 anodes for practical applications faces challenges due to their intrinsic poor electric conductivity (~3×10^{-6} S cm^{-1}) and the capacity decay from pulverization during the charge–discharge process. Building nanostructures with desirable morphology and size is a promising way to address these issues. Generally, electrode materials with nano-sized structures would have a short ion-diffusion path and would provide a large contact area between the electrolyte solution and electrodes. They also accommodate more mechanical strain and structural distortion from lithium insertion/extraction, leading to a high specific capacity and a high rate performance.[2,37,38] Compared to zero-dimensional (0D) nanoparticles, one-dimensional (1D) nanostructures, such as nanowires, nanofibers, and nanotubes, can provide directional electronic and ionic transportation, avoiding disconnection of the nanoparticles and the relatively poor ionic transportation of nanoparticles. Therefore, Viet *et al.*[12] synthesized 1D Nb_2O_5 nanofibers in different polymorphic forms by appropriate heat treatment of the as-spun composite polymeric fibers. XRD analysis shows that H-Nb_2O_5 (500 °C, 1 h), O-Nb_2O_5 (800 °C, 1 h), M-Nb_2O_5 (1000 °C, 1 h), M-Nb_2O_5 (1100 °C, 1 h), and M-Nb_2O_5 (1100 °C, 11 h) were successfully prepared. As observed in the scanning electron microscopy (SEM) and transmission electron microscopy (TEM) images (Fig. 3a–c), the H- and O-phases maintained the usual nanofibrous morphology with an average diameter of around 160 nm, whereas the M-phase adopted submicrometer sized "near-1D" nugget-like morphology. Electrochemical measurement indicates that all of the nanofibrous polymorphs show good cycling stability due to the peculiar porous structure of the electrospun nanofibers; however, their specific capacities differ considerably, depending on their crystal structures (Fig. 3d). M-Nb_2O_5 (1100 °C, 1 h) exhibits the highest capacity, about 242 and 218 mA h g^{-1} during the 2nd and the 25th cycles, respectively, at a current density of 50 mA g^{-1} in the voltage range 1.0–2.6 V (*vs.* Li/Li^+). This is probably due to the facile kinetics of Li-ion intake in M-Nb_2O_5. It was shown that the calculated lithium diffusion coefficients for the H-, O- and M-Nb_2O_5 phases are in the ranges 10^{-17}–10^{-16}, 10^{-15}–10^{-14}, and 10^{-13}–10^{-12} cm^2 s^{-1}, respectively, using a galvanostatic intermittent titration technique (GITT).[39] The nanobelt, another novel 1D nanostructure, is also a promising structure, which could benefit lithium-ion diffusion. Recently, Nb_2O_5 nanobelts with thicknesses of ~15 nm, widths of ~60 nm and lengths of several tens of micrometers were prepared by a hydrothermal method.[40] Electrochemical testing was done in the voltage range 1.2–3.0 V (*vs.* Li/Li^+) under a current density of 100 mA g^{-1}. The first discharge and charge capacities are as high as 250 and 210 mA h g^{-1}, respectively. Furthermore, even at a high current density of 10 A g^{-1}, the capacity still reaches 50 mA h g^{-1}, indicating a high-rate performance. The Nb_2O_5 nanowire superstructure, as an LIB anode, exhibited a high capacity of 177 mA h g^{-1} at a current density of 100 mA g^{-1} and had excellent cycling stability.[41]

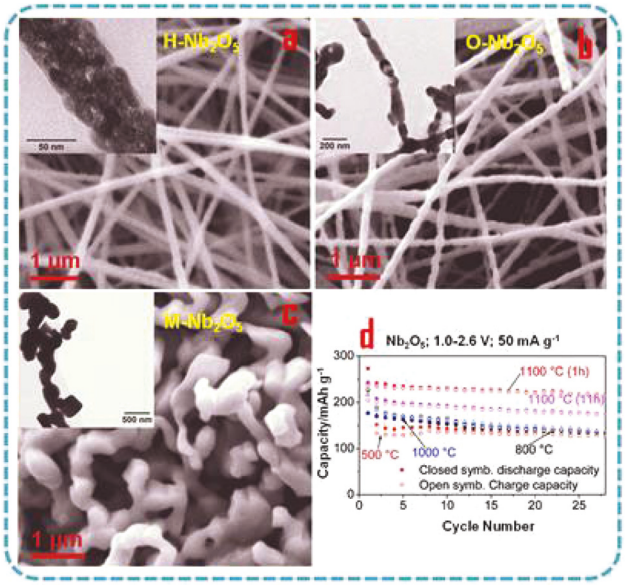

Fig. 3 SEM images of Nb_2O_5 nanofibers annealed in air for 1 h at (a) 500 °C, (b) 800 °C, and (c) 1100 °C (insets: corresponding TEM images). (d) Capacity *versus* cycle number plots of H-, O-, and M-Nb_2O_5. Adapted and reproduced, with permission, from ref. 12. Copyright 2009, American Chemical Society.

Electrodes with 2D nanostructures also deliver remarkable electrochemical performances, due to their large contact areas, enhanced open-edged morphologies and finite lateral sizes.[42–44] As shown in Fig. 4a and b, O-type Nb_2O_5 nanosheets with thicknesses of 50 nm and lengths of 500 nm were produced from the hydrothermal precursor, Nb_3O_7F.[45] The Nb_2O_5 nanosheet anode delivered a superior electrochemical performance with an initial discharge capacity of 184 mA h g^{-1} at a current density of 0.2 A g^{-1}. Meanwhile, a high-rate performance with 90 mA h g^{-1} at 5 C and excellent cycling stability were also observed (Fig. 4c). Additionally, Luo *et al.*[46] also prepared Nb_2O_5 (O- and M-type mixed phase) nanosheets by a simple hydrothermal method using NbO_2 particles as the precursor. An initial discharge capacity as high as 355 mA h g^{-1} was achieved at a current density of 100 mA g^{-1}, and after 40 cycles, the reversible capacity still remained at 185 mA h g^{-1}.

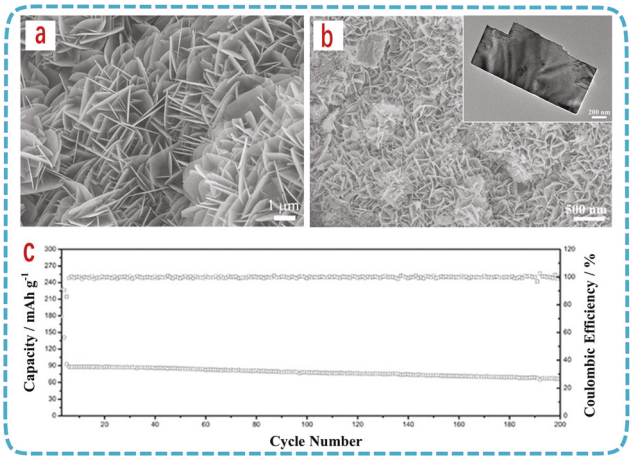

Fig. 4 SEM images of (a) Nb_3O_7F precursor prepared at 160 °C for 24 h and (b) final product, O-Nb_2O_5 (inset: corresponding TEM image). (c) Cycling performance of O-Nb_2O_5 nanosheets under 5 C. Adapted and reproduced, with permission, from ref. 45. Copyright 2015, Nature Publishing Group.

Their superior performance is due to the structure of the nano-chip, which reduces the lithium ion diffusion distance and maintains good contact between the nanosheets and acetylene black.

Hierarchical nanostructures are also highly attractive with regard to application in LIBs.[47–49] As a result, H-Nb_2O_5 hollow nanospheres with an average diameter of ~29 nm and a hollow cavity size of ~17 nm were successfully fabricated, which delivered a high discharge capacity of 197 mA h g^{-1} at a rate of 0.5 C, and the capacity retention could be maintained at around 90% of the initial capacity after 250 cycles.[50] Also, hierarchical flower-like O-Nb_2O_5 microspheres were produced *via* a facile and template-free method.[51] As shown in Fig. 5a, the entire formation process of hierarchical Nb_2O_5 microspheres involves two stages: nucleation and Ostwald ripening. The representative SEM images (Fig. 5b and c) of the product show a large quantity of flower-like microspheres (average diameter of 1.2 μm) constructed from 2D nanoflakes with thicknesses of 30 nm. When evaluated as anode materials for LIBs, Nb_2O_5 microspheres exhibited excellent cycle stability and reversibility, *e.g.*, from 217.5 mA h g^{-1} during the 8th cycle to 219.5 mA h g^{-1} during the 200th cycle at a current rate of 50 mA g^{-1}. Furthermore, a tightly packed vein-like nonporous network of O-Nb_2O_5 was prepared recently by a simple electrochemical anodization process (Fig. 5d).[52] Fig. 5e shows a cross-sectional side view of an annealed Nb_2O_5 film, which consisted of a continuous and tightly packed vein-like nanoporous network. High-magnification observation (Fig. 5f) reveals that the nano-veins have internal diameters ranging from 30 to 50 nm with many lateral interconnections. Such unique structures would provide efficient channels for the fast transfer of both Li-ions and electrons. Hence, the nonporous Nb_2O_5 anode delivered a high reversible capacity of up to 300 cycles at a current density of 0.4 A g^{-1}. The rate performance test

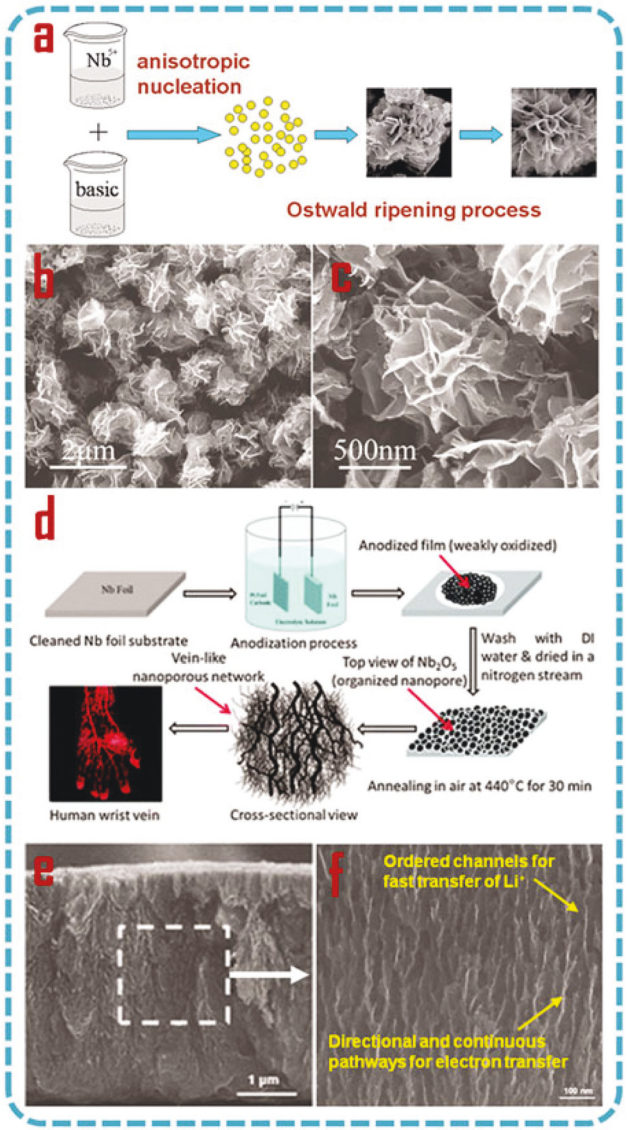

Fig. 5 (a) Schematic formation process of hierarchical flower-like Nb_2O_5 microspheres. (b and c) SEM images of flower-like Nb_2O_5 nanostructures. Adapted and reproduced, with permission, from ref. 51. Copyright 2014, Royal Society of Chemistry. (d) Schematic of the nanoporous Nb_2O_5 preparation procedure. (e and f) SEM images of nanoporous Nb_2O_5 film. Adapted and reproduced, with permission, from ref. 52. Copyright 2013, Royal Society of Chemistry.

showed that a capacity of 141 mA h g^{-1} was obtained at a very high current density of 2.6 A g^{-1}. On the other hand, developing a binder-free Nb_2O_5 electrode directly on the current collector could also enhance the charge transfer significantly, resulting in a superior rate and cycle performance.[14,53,54] For instance, a length of about 1 μm of Nb_2O_5 nanorod array film was prepared by Wen *et al.*[54] through a facile hydrothermal process, and a reversible capacity of about 400 mA h g^{-1} at a current density of 0.2 A g^{-1} was obtained after 50 cycles.

It is well known that poor electronic conductivity limits the diffusion of lithium ions and charge transfer, resulting in a

poor electrochemical performance. When using $Li_4Ti_5O_{12}$ and TiO_2 as anode materials for LIBs, a common way to improve the conductivity is to combine it with other conductive materials, such as amorphous carbon, carbon nanotubes (CNTs) or graphene.[13,55,56] For example, we recently reported that a conforming coating of TiO_2 on CNTs would significantly improve the rate performance and cycle durability, compared with pure TiO_2.[57] Concerning Nb_2O_5 anodes, Kumagai *et al.* firstly introduced graphite into Nb_2O_5 electrodes, so as to increase their electronic conductivities,[35,58] and found that the content of the graphite in the Nb_2O_5 electrode had a marked influence on the cycling behavior. Later, oxygen-deficient niobium oxide immersed in a carbon matrix by a one-step facile hydrothermal synthesis was reported.[59] The carbon matrix and oxygen-deficient niobium oxide could enhance the charge transfer and prevent niobium oxide nanocrystals from pulverization during the charge–discharge process, which could efficiently improve the cycle durability and rate performance. The niobium oxide/carbon matrix structure developed in our group could provide a new design to achieve a high cycle durability and rate performance for low-electronic-conductivity anode materials, especially for TiO_2 and niobium-based oxides.

Besides Nb_2O_5, some other niobium oxides, *e.g.*, NbO_x[17] and $Nb_{12}O_{29}$,[60] were also reported as anode materials for LIBs with promising lithium storage properties. For instance, NbO_x@C nanoparticles were successfully fabricated through the oleylamine-mediated hydrolysis of niobium(v) chloride under solvothermal reaction,[17] and these delivered about 298 mA h g^{-1} after 200 cycles at a rate of 100 mA g^{-1}.

2.2 Li(K)–Nb–O compounds

Rhombohedral $LiNbO_3$, a famous ferroelectric material that is widely used in electro-optics, is also considered to be an interesting anode in LIBs, with a large theoretical capacity of 363 mA h g^{-1} (based on the redox couple, Nb^{5+}/Nb^{3+}, at a voltage of 1.0–1.7 V).[61–63] To improve the kinetics of $LiNbO_3$ for high-power LIB applications, Fan *et al.*[63] developed a superior hybrid anode composed of CNTs and $LiNbO_3$ nanoplates (CNT–$LiNbO_3$). CNTs were used to build a 3D-conductive network and also acted as a backbone to load $LiNbO_3$ nanoplates. As illustrated in Fig. 6a, self-weaving CNT–$LiNbO_3$ hybrids were synthesized using a rhodanine acetic acid-pyrene (RAAP)-directed growth method. RAAP-decorated CNTs are hydrophilic, and the carboxylate groups on RAAP could supply active sites for the sol–gel growth of $LiNbO_3$ nanoplates. An SEM image (Fig. 6b) indicates that the $LiNbO_3$ nanoplates have a lateral dimension of 100–300 nm and are threaded by the CNT networks. Such an architecture can easily achieve rapid electron transport and lithium-ion diffusion (Fig. 6c). After further hybridization with a conductive and elastic polymer of polypyrrole (PPy), a flexible, free-standing CNT–$LiNbO_3$ nanoplate-PPy bulky paper anode was fabricated. As shown in Fig. 6d, the discharge curves of this anode exhibit two different regions corresponding to the complete reduction of Nb^{5+} to Nb^{4+} and the partial reduction of Nb^{4+} to Nb^{3+}, yielding reversible capacities of around 250 mA h g^{-1} at a current density of 0.4 A g^{-1} with a high capacity of 220 mA h g^{-1} remaining after 500 cycles. Moreover, this hybrid anode presents an excellent rate capability (Fig. 6e), *e.g.*, delivering a capacity of 150 mA h g^{-1} at a high rate of 4 A g^{-1}.

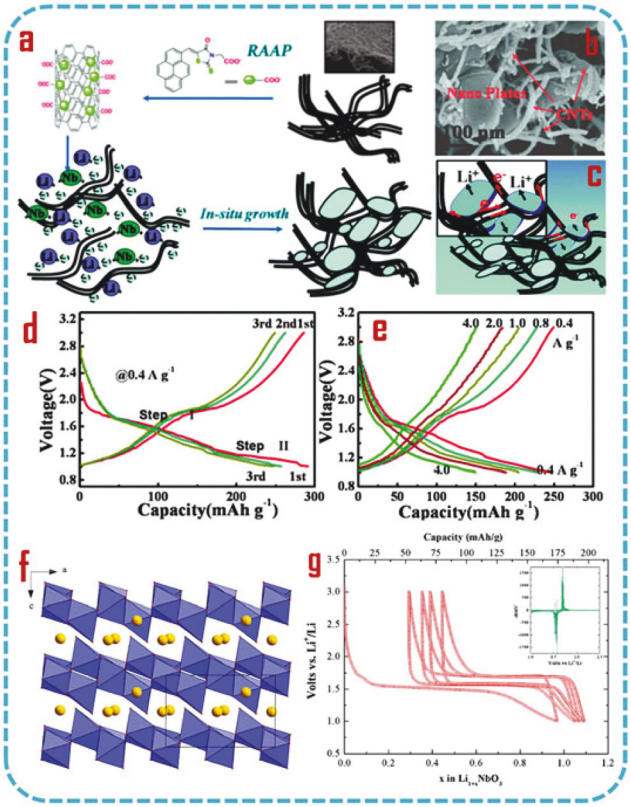

Fig. 6 (a) Schematic synthetic route of self-weaving CNT–$LiNbO_3$ hybrids. (b) SEM image of CNT–$LiNbO_3$. (c) Scheme showing rapid electron transport and Li^+ diffusion in CNT–$LiNbO_3$ hybrids. Charge–discharge profiles of CNT–$LiNbO_3$–Ppy at a low rate (d) and higher rates (e). Adapted and reproduced, with permission, from ref. 63. Copyright 2013, Royal Society of Chemistry. (f) View of the lamellar $LiNbO_3$ structure along *c* (g) Charge–discharge profiles of lamellar $LiNbO_3$ at C/10 (inset: corresponding incremental capacity, d*t*/d*V*, *vs.* potential curve of the 2nd cycle). Adapted and reproduced, with permission, from ref. 64. Copyright 2011, American Chemical Society.

Furthermore, another strategy, a microwave-induced autocombustion reaction, was utilized to fabricate 3D porous $LiNbO_3$ nanocomposites (10–20 nm), which showed a large surface area of 57.8 m^2 g^{-1}, supplying a large interfacial area for electrochemical reactions and enabling lithium-ion transport between the electrode/electrolyte.[59] The electrochemical results demonstrated that this 3D porous $LiNbO_3$ anode delivered a reversible charge/discharge capacity of 200 mA h g^{-1} at 0.5 A g^{-1} and retained 175 mA h g^{-1} after 200 cycles.

In addition to the rhombohedral structure, a new polymorph of $LiNbO_3$ with a lamellar structure (space group: $P2_1/a$), consisting of very similar stacked $[NbO_3]_\infty$ layers along the *c* direction (Fig. 6f), was also developed for reversible lithium intercalation.[64] This was synthesized from a topotactic

reaction of $CuNbO_3$ with eutectic $LiCl/LiNO_3$. The electrochemical behaviour (Fig. 6g) of this new phase is quite attractive, showing the ability to intercalate one Li per formula (*i.e.*, Li_2NbO_3) at a potential of 1.5 V during the first discharge process, and a reversible capacity of 0.7 Li per formula (120 mA h g^{-1}). $LiNb_3O_8$ crystallizes in the monoclinic structure (space group: $P112_1/a$), which is constructed from Nb–O distorted octahedrons with Li atoms occupying partial octahedral sites.[65] Xu *et al.* comprehensively studied 1D porous $LiNb_3O_8$ nanofibers in LIBs, prepared through a simple electrospinning route followed by a post-treatment process.[66] SEM and TEM observations reveal that the $LiNb_3O_8$ nanofibers were polycrystalline, involving many interconnected $LiNb_3O_8$ nanocrystals (~20 nm) and numerous nanosized pores (~18 nm).

Fig. 7a depicts the voltage profiles of the porous $LiNb_3O_8$ anode for the initial two charge–discharge cycles at a current density of 30 mA g^{-1}.[66] The charge–discharge curves could be divided into several regions. During the first discharging, two plateaus (b1–c1 and d1–f1) are clearly observed. In the subsequent charging, the plateaus disappeared and were replaced by an S-shaped curve, which retained its shape during the following cycles. To reveal the lithium storage mechanisms, *in situ* XRD patterns were recorded at various voltage stages during the first cycle (Fig. 7b). During lithiation between points a1–e1, the main peaks moved towards lower angles and the structure of $Li_{1+x}Nb_3O_8$ was maintained. However, at the end of discharging (point f1), the structure of $Li_{1+x}Nb_3O_8$ was destroyed and two new phases (Li_2NbO_3 and Nb_2O_5) were generated. In the subsequent cycles, the XRD patterns remain unchanged, suggesting the reversibility characteristic of intercalation/de-intercalation reactions. Thus, the electrochemical reactions of $LiNb_3O_8$ were proposed as follows:

$$LiNb_3O_8 + 3.6Li^+ + 3.6e^- \rightarrow Li_{2.6}Nb_2O_5 + Li_2NbO_3 \quad (1)$$

$$Li_{2.6}Nb_2O_5 \leftrightarrow Nb_2O_5 + 2.6Li^+ + 2.6e^- \quad (2)$$

$$Li_2NbO_3 \leftrightarrow LiNbO_3 + Li^+ + e^- \quad (3)$$

Furthermore, as promoted by its unique 1D porous nanostructure, this $LiNb_3O_8$ electrode exhibited superior electrochemical properties. It delivered initial discharge capacities of 241.1, 231.2 and 217.0 mA h g^{-1} at current densities of 0.1, 0.5 and 1 C, respectively. After 100 cycles, corresponding specific capacities of 170.1, 141.9 and 119.2 mA h g^{-1} were maintained.

KNb_5O_{13} (orthorhombic *Pbmc* structure) is isostructural with KTa_5O_{13}, which consists of 2D *a*–*b* slabs of edge- and corner-sharing NbO_6 octahedra, and these slabs are interconnected to create a 3D framework.[67–69] Although the K^+ cations reside in the empty channels, there is still room to intercalate Li^+ cations into them, which allows the energy of the Nb^{5+}/Nb^{4+} couple to be probed. The lithiation and delithiation behavior of KNb_5O_{13} at a current of 20 mA g^{-1} is shown in Fig. 8 (middle).[69] Upon discharging, two plateaus (B and D–E) represented two-phase regions, and a solid-solution range, C, was displayed. During the subsequent charging process, an obvious solid-solution range, J, and a large plateau, K–L, were observed. The proposed detailed lithiation/delithiation process is shown in Fig. 8. These experiments demonstrated that only 1D *a*-axis tunnels had access to the electrolyte during lithiation/delithiation, which connected to multiple off-axis sites (4c, 4d, and 8e), resulting in a polarization hysteresis in the potential profile. Additionally, another potassium niobate, $K_6Nb_{10.8}O_{30}$, also exhibited an attractive capacity (around 160 mA h g^{-1}) for reversible Li uptake/removal with a solid-solution range between 0.9 and 1.7 V (*vs.* Li/Li^+).[68]

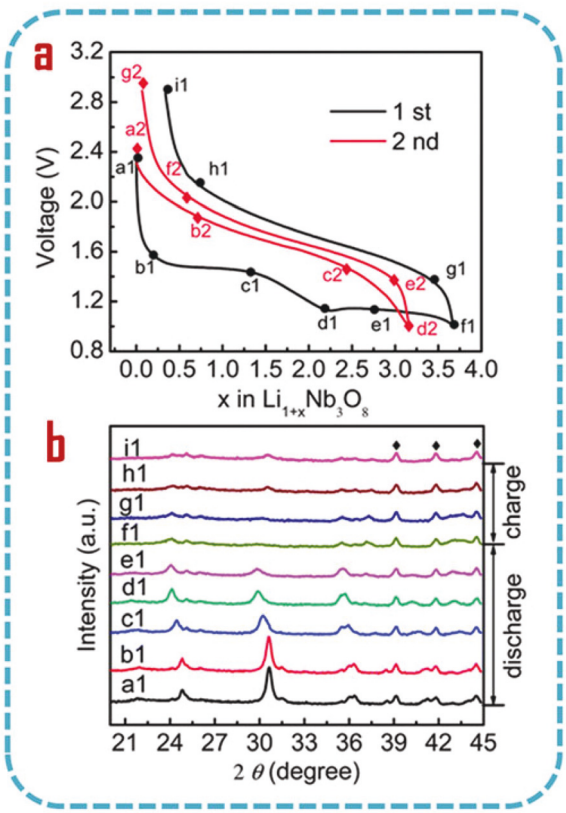

Fig. 7 (a) Voltage-composition profiles of $LiNb_3O_8$ nanofibers. (b) Corresponding *in situ* XRD patterns recorded at various voltage stages during the first cycle. The XRD peaks marked with a diamond shape are assigned to BeO. Adapted and reproduced, with permission, from ref. 66. Copyright 2013, Royal Society of Chemistry.

2.3 Ti–Nb–O compounds

Considering that the atomic radii of niobium and titanium are similar, niobium oxides can form solid solutions with titanium oxides under high temperature calcination.[70] Thus, many types of titanium–niobium oxide compounds, such as $TiNb_2O_7$, $Ti_2Nb_2O_9$ and $Ti_2Nb_{10}O_{29}$, could be formed and used as alternative anode materials for LIBs due to their high lithium storage capacity and safe lithiation potentials (1.7 to 1.0 V *vs.* Li/Li^+).[71–73] Most of these oxides have been used as anode materials for LIBs, especially for $TiNb_2O_7$. Similar to Nb_2O_5, $TiNb_2O_7$ is also a wide-bandgap compound (2.9 eV) and has been used in photo-catalysis applications. $TiNb_2O_7$

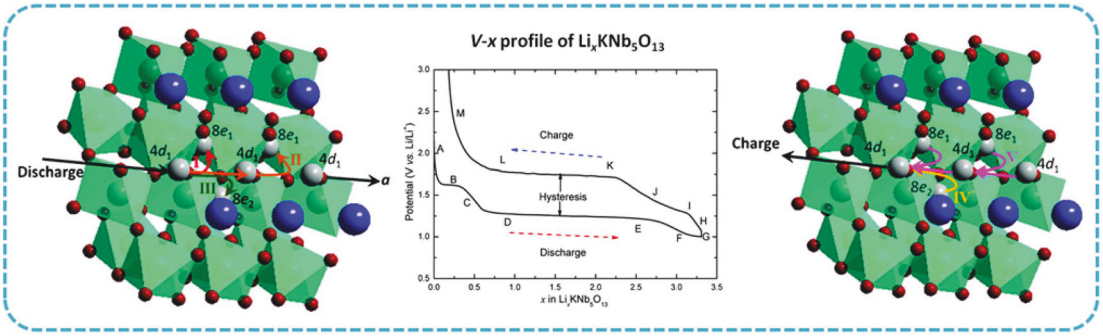

Fig. 8 Proposed lithiation/delithiation model for KNb_5O_{13}. Adapted and reproduced, with permission, from ref. 69. Copyright 2011, American Chemical Society.

belongs to the monoclinic system (space group $C2/m$; unit cell parameters a = 20.351 Å, b = 3.801 Å, c = 11.882 Å, and β = 120.19°). In this monoclinic structure, NbO_6 and TiO_6 octahedra share edges and corners, and the Ti and Nb atoms, located at the central positions of the octahedra, are randomly distributed, while the 2D interstitial space existing in the monoclinic layered structure offers accommodation for up to 5 lithium atoms per unit formula. This five-electron electrochemical reaction corresponds to redox reactions (Ti^{4+}/Ti^{3+}, Nb^{5+}/Nb^{4+} and Nb^{4+}/Nb^{3+}) that deliver a high theoretical capacity of 387.6 mA h g^{-1}, almost twice than that of $Li_4Ti_5O_{12}$. Lithium insertion and extraction in $TiNb_2O_7$ was initially studied by Cava *et al.*[74] It was found that the structure could be retained (volume change 3.6%) during the electrochemical process of lithium insertion and extraction. *In situ* XRD showed that the volume of the crystal increases from 0.794 to 0.833 nm^3 after the charging process, and could revert back to 0.794 nm^3 after the discharging process, indicating that $TiNb_2O_7$ exhibits excellent cycle durability. Density functional theory (DFT) calculations, and light and dark field electron microscopies were used for an in-depth investigation of the mechanism of lithium insertion and extraction in $TiNb_2O_7$. It was found that lithium ions were stored in the (001) plane of $TiNb_2O_7$, and the distance between the (001) planes increased from 1.03 nm to 1.15 nm.[75] The high cycle durability resulting from the small volume change during the charge–discharge process and the high theoretical capacity of $TiNb_2O_7$ makes it a very promising anode material for LIBs. Recently, carbon-coated $TiNb_2O_7$ ($TiNb_2O_7$/C) and Nb (10%)-doped $Ti_{0.9}Nb_2O_7$ ($Ti_{1.1}Nb_{2.1}O_7$) were tested as anodes for LIBs,[71,76] as shown in Fig. 9. The initial discharge capacity of $TiNb_2O_7$/C was 285 mA h g^{-1} at 0.1 C with no capacity loss after 40 cycles. Besides, a plateau at 1.6 V was also observed. Even more importantly, these materials also exhibited excellent rate performances and about 150 mA h g^{-1} at a current density of 2C under a potential window of 1.4–2.5 V. Also, doping Nb for Ti could improve the intrinsic conductivity, which would improve the performance. Considering the flat potential plateau for $TiNb_2O_7$, a 3 V full cell with $TiNb_2O_7$ as anode and $LiMn_2O_4$ as cathode was proposed by Goodenough *et al.*, and this full cell exhibited an excellent cycling performance.[76]

In general, the formation temperature of $TiNb_2O_7$ is fairly high (900–1100 °C), resulting in $TiNb_2O_7$ having a low surface area, which could decrease the kinetics of lithium diffusion.

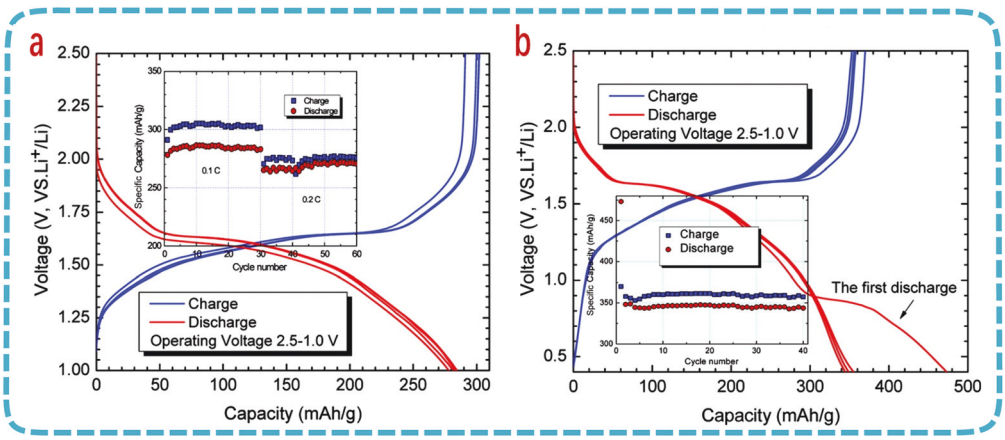

Fig. 9 (a) Charge/discharge curves of the $TiNb_2O_7$/C anode at 0.1 C, cycled between 1.0 and 2.5 V, together with its capacity retention over 30 cycles; (b) Charge/discharge curves of the $TiNb_2O_7$/C anode at 0.1 C, cycled between 0.4 and 2.5 V, together with its capacity retention over 40 cycles. Adapted and reproduced, with permission, from ref. 71. Copyright 2011, American Chemical Society.

Therefore, it is necessary to prepare $TiNb_2O_7$ with a high surface area. Recently, we prepared $TiNb_2O_7$ nanoparticles with a particle size of 10 nm using an SBA-15 template.[77] The capacity of $TiNb_2O_7$ with a smaller particle size was about 250 mA h g^{-1} at 0.5 C, with a high coulombic efficiency (above 98% over 300 cycles). The enhanced electrochemical performance of $TiNb_2O_7$ nanoparticles is attributed to its high surface area, which not only increases the contact area between the electrolyte and the electrode material but also reduces the lithium diffusion path. Beyond the $TiNb_2O_7$ nanoparticles, $TiNb_2O_7$ with an ordered mesoporous structure not only provides a high surface area but also provides extra channels for lithium ion diffusion. $TiNb_2O_7$ with a mesoporous structure, synthesized by assisted self-assembly of a block copolymer, has a particle size of 15 nm and a pore size of 40 nm. Due to its relatively large specific surface area, capacities of 289, 162, and 116 mA h g^{-1} were obtained at 0.1, 20 and 50 C, respectively. The retention ratio remains around 81% after 2000 cycles at 10 C.[78] Guo *et al.* used F127 as a template to prepare a porous structure of $TiNb_2O_7$; an excellent cycle performance with a capacity retention rate of 84% and a rate-reversible capacity of 200 mA h g^{-1} was obtained after 1000 cycles at 5 C.[79] Qian *et al.* also used P123 as a template to prepare $TiNb_2O_7$ porous nanospheres.[80] Preparing $TiNb_2O_7$ with a rich porosity with the assistance of templates, such as F127, SBA-15, and block copolymers, would increase the production cost and complexity. Hierarchical $TiNb_2O_7$ microspheres were synthesized by a one-step facile and low-cost solvothermal synthesis.[81] The morphology and elemental distribution can be seen in Fig. 10.

Therefore, the $TiNb_2O_7$ microspheres with a hierarchical porous structure exhibit an exceptionally high rate capability and an excellent cycling performance. Besides, $TiNb_2O_7$ nanofibers with a diameter of ~100 nm were fabricated by a simple electrospinning method;[82] after calcination at high temperature, a "nano-pearl" morphology was prepared, as shown in Fig. 11.

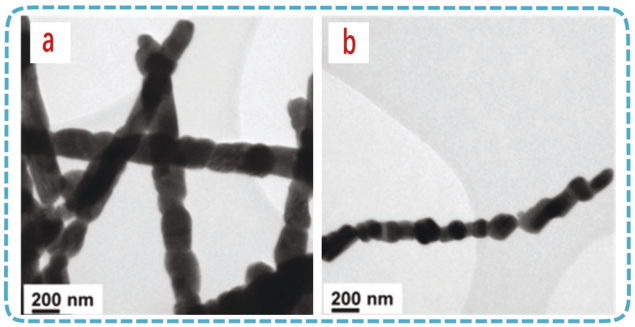

Fig. 11 (a, b) Bright-field TEM images of $TiNb_2O_7$ nanofibers with a "nano pearl" structure. Adapted and reproduced, with permission, from ref. 82. Copyright 2011, WILEY-VCH Verlag GmbH & Co. KGaA, Weinheim.

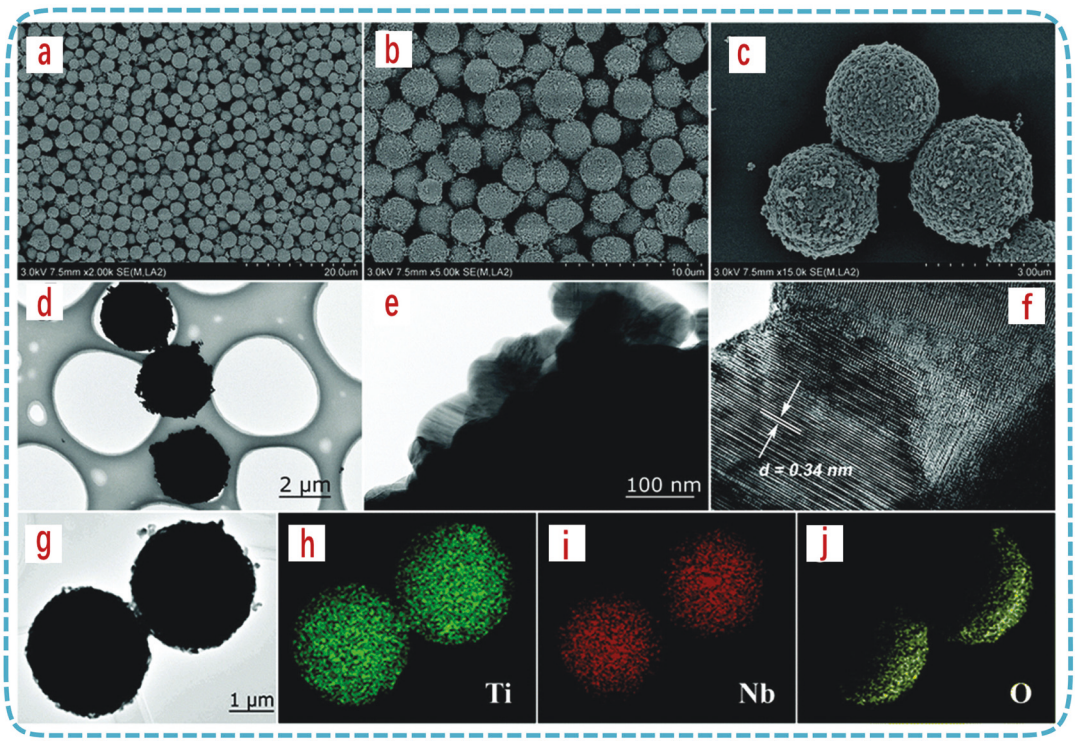

Fig. 10 (a–c) FESEM images; (d–f) TEM images of the as-prepared $TiNb_2O_7$ microspheres; (g) STEM image; (h–j) EDX elemental mapping of the area of (g), for titanium, niobium, and oxygen, respectively. Adapted and reproduced, with permission, from ref. 81. Copyright 2011, Royal Society of Chemistry.

This novel nanostructured material with nano-pearl morphology exhibited a high rate capacity (85 mA h g^{-1} at 50 C) and good capacity retention, since this 1D nanostructure had favorable kinetic properties. An excellent electrochemical performance for $TiNb_2O_7$ with 1D nanofibers, prepared by electrospinning, was also obtained by Ramakrishna *et al.*[83] while $TiNb_2O_7$ nanorods prepared by a simple sol–gel method also exhibited excellent rate and cycle durability.[84] Actually, $TiNb_2O_7$ with a band gap of 2.7 eV shows poor electronic conductivity; however, fast lithium-ion and electron conductivity are necessary for LIBs with a high electrochemical performance. Doping elements into $TiNb_2O_7$ is a general strategy for improving the conductivity. For example, ruthenium-doped $TiNb_2O_7$, $Ru_{0.01}Ti_{0.99}Nb_2O_7$, delivered an enhanced lithium-ion diffusion coefficient and electronic conductivity, resulting in an improved electrochemical performance.[85] However, considering the high price of the ruthenium precursor, it is still a challenge to improve the conductivity of $TiNb_2O_7$ using a low-cost doping strategy. Combination with conducting materials or coating conductive materials on $TiNb_2O_7$ would be another way to improve the conductivity; for example, a $TiNb_2O_7$/graphene composite could be developed.[86] It is reported that porous $TiNb_2O_7$ nanofibers decorated with conductive TiNbN bumps could significantly improve the electrochemical performance.[87] Recently, partial nitridation of $TiNb_2O_7$ was thought of as a practical way to improve the performance of LIBs. The porous structure and conducting $Ti_{1-x}Nb_xN$ layer on porous $TiNb_2O_7$ enhanced the transport kinetics associated with lithium ions and electrons, resulting in a high discharge capacity of 265 mA h g^{-1}, a remarkable rate capability and an excellent cycle durability (about 91% capacity retention compared to the initial value after 1000 cycles at 5 C).[88]

Recently, $Ti_2Nb_{10}O_{29}$, another typical titanium–niobium oxide, was also developed as an anode material for LIBs.[89–91] As a powerful technique to investigate the mechanism of lithium insertion and extraction, *in situ* XRD showed that the electrochemical reaction of $Ti_2Nb_{10}O_{29}$ at a high potential window (1.6–3.0 V) and a low potential region (1.0–1.5 V) is a solid solution reaction, while the platform area (1.4–1.6 V) is a region of two-phase coexistence.[72] The good rate performance of $Ti_2Nb_{10}O_{29}$ was attributed to the open ReO_3 structure. Recently, employing $Ti_2Nb_{10}O_{29}$ as anode and $LiFePO_4$ as cathode, a full cell exhibited high coulombic efficiency and excellent cycle durability, indicating that $Ti_2Nb_{10}O_{29}$ could be used as an anode in commercial LIBs.[92] $TiNb_6O_{17}$, with a similar crystal structure to $Ti_2Nb_{10}O_{29}$, has also been applied as an anode material for LIBs with a fair electrochemical performance.[93]

2.4 Other niobium-based oxide (M–Nb–O, M = V, Al, and W)

Introducing elemental vanadium into the Nb_2O_5 pure phase can increase the theoretical capacity of Nb_2O_5. Therefore, V_2O_5 and Nb_2O_5 composites with different ratios were developed as anode materials for LIBs. $NbVO_5$ with a high ratio of V_2O_5 to Nb_2O_5 showed a poor rate performance.[94] Only composites with a lower V_2O_5 concentration (10 wt%) exhibited an acceptable capacity of 200 mA h g^{-1} at a current density of 100 mA g^{-1}. Tetragonal $VNb_9O_{24.9}$-based nanorods were synthesized through an aerosol-assisted process.[95] This new form in a V–Nb–O system showed an outstanding cycling stability as well as a moderate rate capability. The electrochemical properties are consistent with the unique susceptibility of the structure to intercalate lithium reversibly. This specific effect after introducing vanadium can improve the performance and cycle stability. Current research on vanadium and niobium oxide composites is limited, but its superior electrochemical performance should attract more and more attention from researchers around the world.

The lithium ion insertion and extraction behavior of $AlNbO_4$ was initially investigated by Zachau *et al.*[96] and the capacity of these materials were dependent on the operation temperatures due to the poor delithiation dynamic kinetics. It was shown that only 0.1 mol Li^+ can be embedded per mole $AlNbO_4$ at room temperature.[97] Although an enhanced electrochemical performance was obtained for $AlNbO_4$ nanoparticles with an average size of 15–20 nm, $AlNbO_4$ materials still have many problems, such as a poor rate capability and an initial irreversible capacity loss. The lithium ion insertion and extraction behavior of the Nb_2O_5–WO_3 system were also investigated.[98–100] Interesting results were also obtained in that niobium substitution of tungsten could accelerate lithium ion diffusion in the bulk phase.

3. Niobium oxides for sodium-ion batteries (SIBs)

Sodium-ion batteries are considered to be promising candidates for large-scale applications because of their low cost and huge availability of sodium salts. The basic principle of a sodium-ion battery is the same as that of LIBs. However, the performance reported for sodium-ion batteries is much lower than that for LIBs due to the inferior resistance between Li and Na, resulting in a low energy density and sluggish kinetics of Na-ion diffusion. Therefore, it is necessary to find a proper electrode that can provide sufficient energy/power density and cycle stability. Up to now, only one paper has reported the use of Nb_2O_5 as an anode for a sodium-ion battery. A composite consisting of niobium oxide and carbon delivered a reversible capacity of ~175 mA h g^{-1} and provided an excellent rate performance and cycle stability for up to 300 cycles.[7] The Na-ion de/intercalation mechanism in the Nb_2O_5 crystal structure is summarized in Fig. 12. $Na_xNb_2O_5$ is formed after Na ions are inserted into Nb_2O_5 during the first discharge (>0.3 V *vs.* Na); during the discharge process at low potential (<0.3 V *vs.* Na), $Na_xNb_2O_5$ would partially transform into NbO and Na_2O, accompanied by amorphization through further sodiation. In this process, the storage of Na-ions in the amorphous $Na_xNb_2O_5$ phase (x = 1.34) could be completed through capacitive reactions. The Na deintercalation reactions, which form amorphous $Na_yNb_2O_5$ (y = 0.28) *via* capacitive reactions could be completed by the subsequent charge process, whereas NbO and Na_2O remain unchanged.

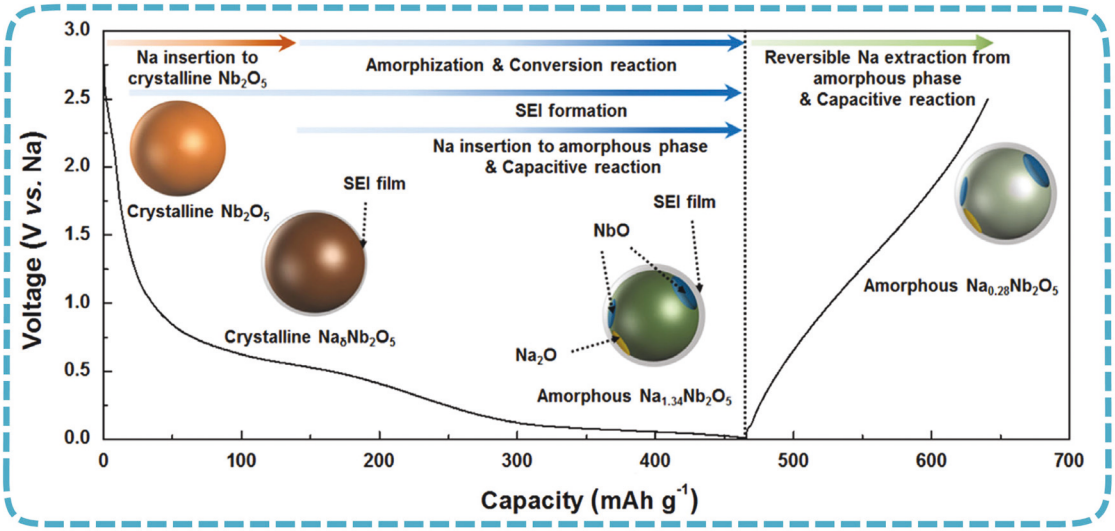

Fig. 12 Schematic of the Na storage behavior in Nb_2O_5 electrodes. Adapted and reproduced, with permission, from ref. 7. Copyright 2015, Elsevier.

4. Niobium oxides for vanadium redox flow batteries

Unlike lithium-ion and sodium-ion batteries, vanadium redox flow batteries (VRBs) store or release energy in two separate liquid reservoirs, employing two soluble VO^{2+}/VO_2^{+} and V^{2+}/V^{3+} redox couples in sulphuric acid as the positive and negative half-cell electroactive species, respectively. The redox chemistry is shown as follows:[101–104]

$$\text{Positive}: \ VO_2^{+} + 2H^{+} + e^{-} \leftrightarrow VO^{2+} + H_2O \quad E^{\circ} = 1.0 \text{ V } \textit{vs.} \text{ SHE} \tag{4}$$

$$\text{Negative}: \ V^{2+} \leftrightarrow V^{3+} + e^{-} \quad E^{\circ} = -0.26 \text{ V } \textit{vs.} \text{ SHE} \tag{5}$$

$$\text{Overall}: \ VO_2^{+} + V^{2+} + 2H^{+} \leftrightarrow VO^{2+} + V^{3+} + H_2O \quad E^{\circ} = 1.26 \text{ V} \tag{6}$$

In VRBs, these vanadium redox reactions take place on the surface of electrodes (*e.g.*, graphite felt, carbon felt, or carbon paper), without structural changes, by providing only redox-active sites. However, these pristine carbon-based electrode materials demonstrate low electrochemical activity and poor kinetic reversibility, which limit the power performance of VRBs. Therefore, modification of the carbon-based materials is necessary to improve the electrocatalytic activity, for example, attaching functional groups, such as carboxylic, hydroxyl, and pyridinic nitrogen groups,[105–107] on the surface, or coating (or depositing) noble metals (*e.g.*, Pt, Au, Pd, Ir, and Ru) and metal oxides (*e.g.*, Mn_3O_4, WO_3, PbO_2, and Nb_2O_5) onto carbon-based electrodes.[108–111] Among these, low-cost Nb_2O_5 shows a promising catalytic effect in VRBs.[112]

Recently, Li *et al.*[112] reported the use of Nb_2O_5 and W-doped Nb_2O_5 nanorods as electrocatalysts deposited on the surface of graphite felts (GFs) to enhance the electrochemical activity of electrodes in a VRB system. The samples were prepared by hydrothermal treatment at 170 °C for 48 h, in which the GFs were placed in a Teflon-sealed autoclave containing ammonium niobium oxalate solutions or ammonium paratungstate, followed by calcination at 500 °C in Ar. The amount, size, and distribution of the Nb_2O_5-based nanorod catalysts on GF surfaces were investigated. It was found that the addition of a small amount of a W source in the precursor solution could promote the precipitation of the active materials, and the obtained W-doped Nb_2O_5 had much smaller particle sizes and a more uniform size distribution. As demonstrated in Fig. 13b, the optimized product (*i.e.*, W-doped Nb_2O_5 prepared with a 0.05 M Nb concentration in the precursor solutions, abbreviated as 0.05 M-Nb(W)) shows small nanoparticles with sizes of around 250 nm, which are composed of many nanorods uniformly distributed on GFs. The charge–discharge voltage profiles at a current density of 150 mA cm^{-2} for the pristine, Nb_2O_5-modified (0.10 M-Nb) and W-doped Nb_2O_5-modified (0.05 M-Nb(W)) GF electrodes are displayed in the inset of Fig. 13b. The overpotentials significantly decreased as a result of introducing Nb_2O_5 and W-doped Nb_2O_5, resulting in a lower charge voltage and a higher discharge voltage, which have a critical influence not only on the redox reaction kinetics but also on the charge transfer. AC impedance analysis confirmed that the 0.05 M-Nb(W) sample has the lowest charge transfer resistance. Compared with the pristine GF electrodes, the energy efficiency (EE) of VRBs was improved by 7.6 and 10.7% for the 0.10 M-Nb and 0.05 M-Nb(W) samples, respectively, and the 0.05 M-Nb(W) electrode delivered the highest specific discharge capacity of 14.4 Ah L^{-1} at 150 mA cm^{-2} (about 1.8 times higher than the pristine GF electrode). These results indicate that Nb_2O_5-based nanorods (especially for W-doped Nb_2O_5) offer great promise as high-performance

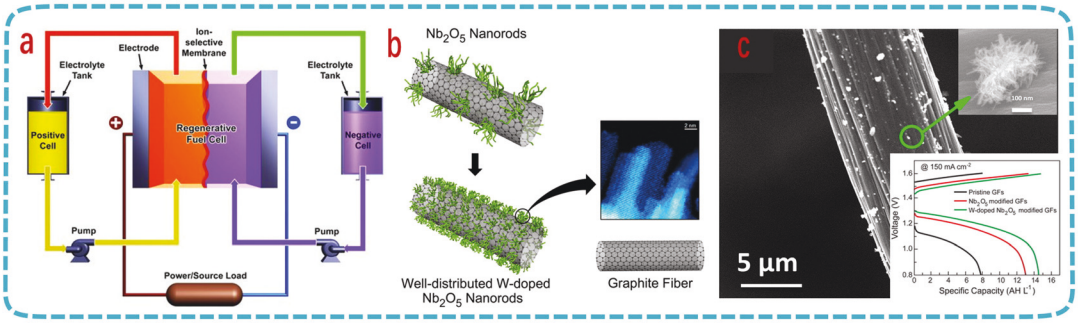

Fig. 13 A schematic of the structure of a redox flow battery. Adapted and reproduced, with permission, from ref. 112. Copyright 2013, American Chemical Society, and from ref. 113. Copyright 2011, WILEY-VCH Verlag GmbH & Co. KGaA, Weinheim.

electrocatalysts toward both VO^{2+}/VO_2^+ and V^{2+}/V^{3+} redox couples to enhance the electrochemical activities of the GF electrodes for VRB applications.

5. Niobium oxides for hybrid supercapacitor

Supercapacitors with high power and long durability could be promising candidates for solving the energy crisis. In electric double-layer capacitors (EDLCs), both positive and negative electrodes used activated carbon, which inevitably restricts their energy densities, specific capacitances and working voltage window, even though they have the advantages of a high power density and excellent cycle durability.[114] Hence, it is necessary to improve the energy density of EDLCs so that they can meet the needs of commercial applications. Hybrid supercapacitors, consisting of metal–oxide positive electrodes with pseudocapacitive behavior and activated-carbon negative electrodes with EDLC behavior are an efficient way to increase the energy density of EDLCs.[115] The operation mechanism of this hybrid supercapacitor is that the charge is stored in the positive electrode by a reversible non-faradaic reaction, such as with Li^+ and Na^+, on the surface of activated and porous carbon material, whereas a reversible faradaic reaction occurs on the metal–oxide electrode. Supercapacitors with this asymmetric configuration can accumulate charge through a faradaic redox electrochemical reaction process, which can contribute to the enhanced specific capacitance and extended working voltage window, leading to an increase in the energy density of the hybrid capacitor. This state-of-the-art hybrid supercapacitor shows an improved energy density, an excellent cycle life, and a high working voltage. RuO_2 has been extensively investigated as the electrode material in hybrid supercapacitors, since it provides superior specific capacitance, cycling stability, and conductance;[116] however, the high cost of this material limits its application in hybrid supercapacitors.

Recent studies demonstrated that the capacity of bulk Nb_2O_5 was higher than that of conventional $Li_4Ti_5O_{12}$ at high rates, indicating that it exhibited the electrochemical features of a pseudocapactor.[117] As we mentioned above, the pseudocapacitance only occurred on the surface of Nb_2O_5, rather than the bulk crystal. Recently, DFT calculations showed that a solid solution formed at specific sites by intercalating atoms (lithium) could donate electrons locally to its neighboring atoms, resulting in the reduction of niobium, and the nanoporous structure could be the origin of the high-rate pseudocapacitance in these pseudocapacitor materials.[118] These results also showed that Nb_2O_5 with a nano-porous structure could improve the performance. Actually, the highest specific capacity was obtained with the orthorhombic Nb_2O_5 phase, among various crystal structures of Nb_2O_5. However, the formation of this specific structure at a high calcination temperature (>600 °C) could lead to nanoparticle aggregation. Such aggregation of Nb_2O_5 nanoparticles would limit application in devices that require high-power electrode materials to balance the kinetics gap between the slow faradaic anode and the fast electric double-layer-type cathode. Nanosized orthorhombic Nb_2O_5 was regarded as a highly advantageous material for improving the kinetics in the anode system. In spite of this merit, one of the major challenges is the synthesis of small-sized orthorhombic Nb_2O_5 nanoparticles. A mesoporous Nb_2O_5/carbon (M-Nb_2O_5–C) nanocomposite anode was synthesized by a simple one-pot method using a block-copolymer-assisted self-assembly,[119] as shown in Fig. 14. The asymmetric CV curves (Fig. 14a and b) of these hybrid supercapacitors, using M-Nb_2O_5–C as electrode, clearly indicated that a faradaic reaction happened in the supercapacitor system. Besides, the linear relationship between the current and scan rates (Fig. 14c) also revealed that the surface faradaic reactions, rather than the diffusion-limited reactions, dominated the charge-storage reactions in the supercapacitor system, which delivered a high specific capacity with an excellent rate performance and cyclability (~90% at 1000 mA g^{-1} after 1000 cycles) and outstanding energy and power densities (74 Wh kg^{-1} and 18 510 W kg^{-1}). Nb_2O_5@carbon core–shell nanocrystals (Nb_2O_5@C NCs) with controlled crystalline phases (orthorhombic (T) and pseudohexagonal (TT)) were also produced by a one-pot microemulsion method.[120] The appropriate pH conditions in the water-in-oil microemulsion system play a most important role in the control of the Nb_2O_5 crystalline phases. Acidic and alkaline conditions led to T-Nb_2O_5@C and TT-Nb_2O_5@C NCs, respectively.

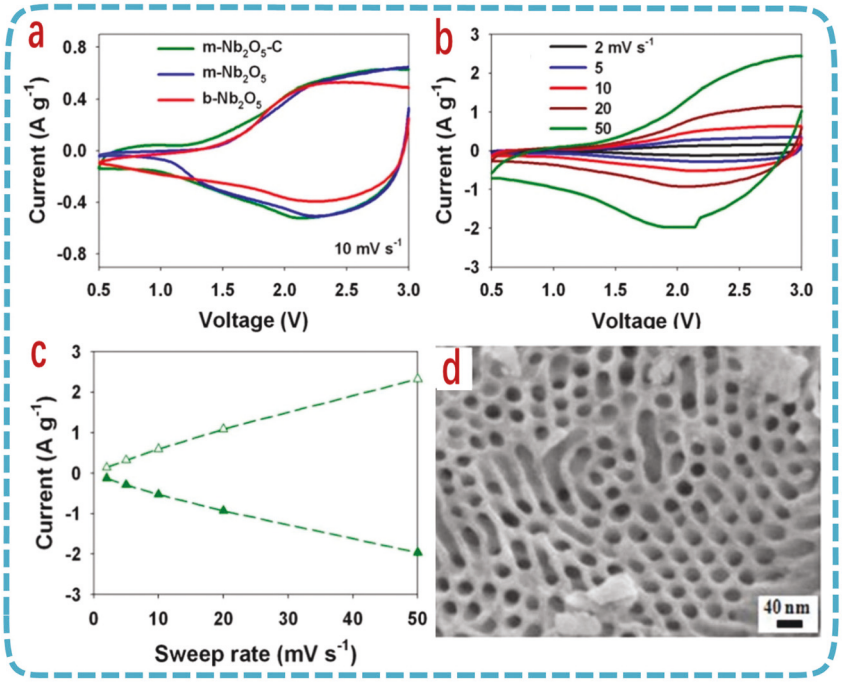

Fig. 14 (a) CV curves of hybrid supercapacitors based on M-Nb_2O_5–C, M-Nb_2O_5, and b-Nb_2O_5 anodes at a scan rate of 10 mV s^{-1}; (b) CV curves of a hybrid supercapacitor using an M-Nb_2O_5–C anode at various scan rates from 2 to 50 mV s^{-1}; (c) specific peak current of hybrid supercapacitor based on an M-Nb_2O_5–C anode with respect to various sweep rates from 2 to 50 mV s^{-1}; and (d) SEM image of M-Nb_2O_5–C. Adapted and reproduced, with permission, from ref. 119. Copyright 2011, American Chemical Society.

The T-Nb_2O_5@C showed rapid rate capability compared to that of TT-Nb_2O_5@C and carbon shell-free Nb_2O_5 NCs due to the synergistic effects of (i) the structural advantages of T-Nb_2O_5 and (ii) the conductive carbon shell, which promoted high electron mobility. The obtained high performance of the T-Nb_2O_5@C core/shell nanocrystals indicates that combination with conducting materials could enhance the charge transfer and increase the rate capability. Therefore, ongoing research on Nb_2O_5 as an electrode for a supercapacitor involves combining conducting carbon materials to improve the charge transfer. T-Nb_2O_5/graphene and Nb_2O_5/CNTs exhibited excellent power densities and cycle performance.[15,42,55,110,121,122] For example, a composite consisting of nano-sized Nb_2O_5 and highly conductive CNTs was prepared by Lu *et al.*;[15] a T-Nb_2O_5/graphene nanocomposite was also successfully prepared by a hydrothermal and heat-treatment process.[42] The use of graphene or carbon nanotubes as an effective conductive support could significantly improve the conductivity of the electrode, lower polarization, and enhance the power density. Both Nb_2O_5/CNTs and Nb_2O_5/graphene exhibited enhanced intercalation pseudocapacitance and excellent high rate capability. It was reported that a microporous carbide-derived carbon composite (CDC) exhibited the highest specific surface area (up to more than 3000 m^2 g^{-1}),[123] therefore, a niobium pentoxide and carbide-derived carbon composite (Nb_2O_5/CDCs) with a layered structure was prepared by a hydrothermal method.[122] Developing a facile way to prepare orthorhombic-phase niobium oxide (T-Nb_2O_5) is another direction in research into the use of Nb_2O_5 as a supercapacitor. Recently, T-Nb_2O_5 nanowires with an ultra-thin carbon coating were prepared by a facile hydrothermal method, and such material exhibited excellent Li^+ storage ability.[8] Kong *et al.* developed a facile and sustainable method to prepare T-Nb_2O_5 nanocrystals using novel nanorod-like cellulose nanocrystals (CNs) as soft templates.[124] The T-Nb_2O_5 nanocrystals exhibited unprecedented Li^+ intercalation pseudocapacitance and an excellent cycle performance.

Free-standing binder-free electrodes have been extensively used for bendable, wearable, and portable electronics. After employing these electrodes, which consist of high-capacitance components and good ionic electric conductive pathways, such devices delivered a high volumetric capacitance and provided as much energy as possible in a rather limited space. The hydrothermal reaction of Nb_2O_5 with 2D flexible graphene is a possible way to fabricate a free-standing Nb_2O_5/graphene paper electrode,[9] as shown in Fig. 15. From the SEM images (Fig. 15a–f), each paper electrode consisted of compact layers and channels between layers, which can enhance the ion diffusion. Nb_2O_5 nanodots with an average size of 1–3 nm were uniformly dispersed on the graphene nanosheets, as shown clearly in the TEM images (Fig. 15g–i).

$TiNb_2O_7$ was also developed as an electrode material for supercapacitors.[125–127] Recently, a hybrid supercapacitor consisting of porous $TiNb_2O_7$ nanotubes[125] delivered a high energy density of ~74 Wh kg^{-1}. Madhavi *et al.* demonstrated that a hybrid supercapacitor with a $TiNb_2O_7$ nanofiber

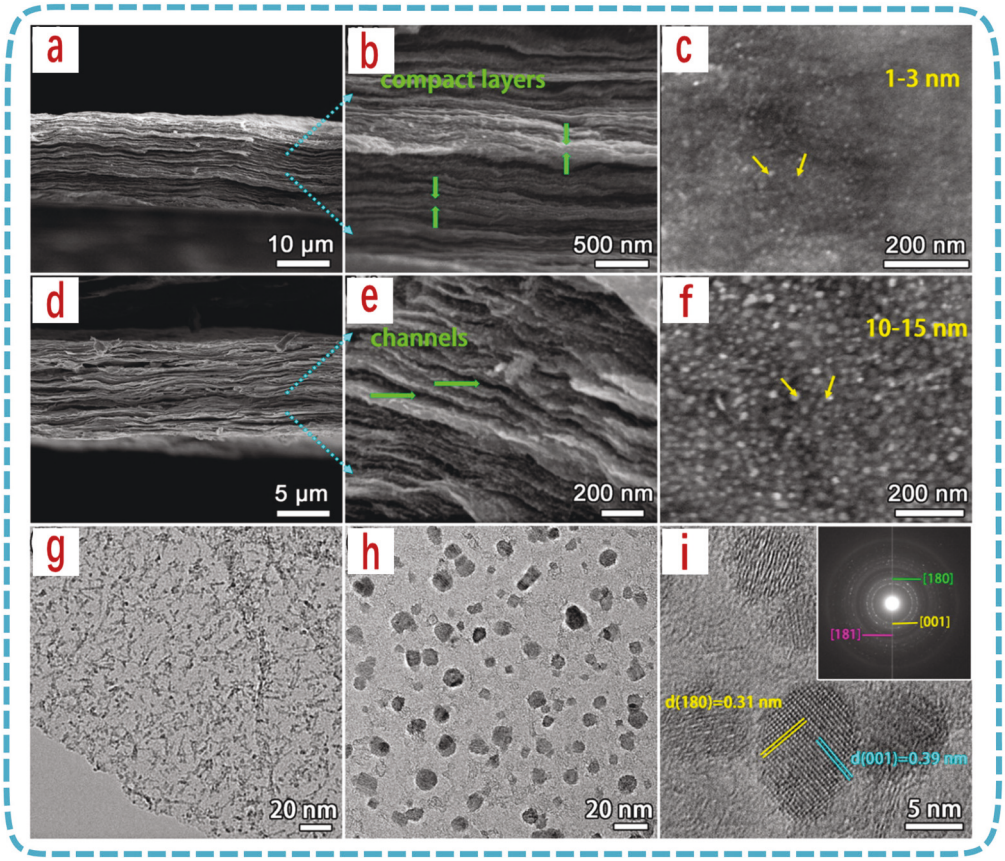

Fig. 15 Cross-sectional and top-view SEM images of Nb_2O_5/rGO (a–c) and T-Nb_2O_5/graphene composite papers (d–f) and TEM image of Nb_2O_5/rGO (g). TEM image (h) and HRTEM and electron diffraction pattern (i) of T-Nb_2O_5/graphene. Adapted and reproduced, with permission, from ref. 9. Copyright 2011, American Chemical Society.

electrode delivered high energy (43 Wh kg^{-1}) and power densities (3 kW kg^{-1}), as well as a good cycle ability (84% of the initial value after 3000 cycles).[128] Besides, the selectivity of the electrolyte solution is another issue concerning the application of Nb_2O_5 as a supercapacitor. Recent research showed that the highest capacitance and coulombic efficiency could be achieved using an electrolyte containing 1 M lithium perchlorate in ethylene carbonate/dimethyl carbonate.[122]

6. Niobium oxides as electrochemical support for fuel cells

Due to the importance of energy conversion and concerns about global warming and climate change caused by carbon emissions from the burning of fossil fuels, the development of efficient and clean fuels is urgently needed and worthwhile for future generations.[129–132] One way to solve this dilemma is to use hydrogen-based fuel cells.[6,133] Compared to other current and conventional energy conversion systems, fuel cells are considered as a non-polluting power source that provides much higher energy efficiency and energy density as well as having the advantage of very low or even zero emissions of harmful greenhouse gases. Therefore, fuel cells have attracted a lot of interest in science and engineering.[134–137] Fuel cells are electrochemical devices that convert chemical energy (such as hydrogen and methanol) into electricity by the electrochemical reaction of positively charged protons with an oxidizer (air or pure oxygen). The basic configuration of fuel cells consists of an anode, a cathode, and an electrolyte. The main goal of current fuel cell technology is to reduce the costs and to deliver high performance and durability, since current fuel cell systems, which have a high cost and relatively poor durability, cannot meet the targets laid out by the Department of Energy (DOE).[138–140] However, the main cost in a fuel cell system is associated with the cathode side, where sluggish oxygen-reduction reactions occur. The ongoing ways to reduce cost and improve the performance of the oxygen-reduction reaction can be generally classified as:[139,141–155] (a) reduction of the catalyst loading in the fuel cell electrode while maintaining a high performance; (b) development of a metal alloy with a different morphology and high performance to reduce platinum loading; (c) reduction of the catalyst particle size to expose a larger surface area for the oxygen reduction reaction; (d) development of non-noble-metal catalysts, such as nitrogen, sulfur and phosphorus-doped carbon materials, such as

porous carbon, carbon nanotubes, and graphene; (e) development of transition-metal oxides and carbon composites as low-cost catalysts; and (f) improvement of the performance of carbon-based electrochemical supports and development of new non-carbon catalyst support materials, such as metal oxides, nitrides or carbides. As clean energy systems, proton exchange membrane fuel cells (PEMFCs) and direct methanol fuel cells (DMFCs) have been extensively studied during the past two decades.[129,156–158] Although these two promising devices have achieved significant progress and could be commercially available for vehicles (Toyota Mirai, Honda FCX Clarity and Hyundai Tucson Fuel Cells), the chargers and other portable devices, the high costs (mainly from the catalyst), and the durability issues still limit their large-scale application. Compared with other catalysts, platinum provides the benefits of high catalytic activity, chemical stability in acid solution, high exchange current density and superior performance;[159] therefore, high-cost platinum and platinum-based alloys are common catalysts in PEMFCs and DMFCs. It is essential to reduce the platinum loading and to improve the efficiency of PEMFCs and DMFCs. Compared to bulk metal catalysts without supporting materials, it is well known that nano-sized platinum catalysts supported by other materials are effective in improving stability and performance.[160] Good electrochemical support, especially when it can provide good interaction between the catalyst and the support, could improve the efficiency of the catalyst and reduce catalyst loading. In addition, it can modify the energy levels of electrons in platinum, leading to a sufficiently improved catalyst performance and durability. Moreover, it can reduce catalyst poisoning (such as carbon monoxide), and in some cases, it affects the catalyst particle size.[161,162] For example, the particle size of platinum on nitrogen-doped carbon nanotubes (N-CNTs) is much smaller than that on pure carbon nanotubes, although these two types of carbon nanotubes exhibited almost the same surface area and the mass loading of platinum was the same.[163] The strong connection between platinum and N-CNTs results in a smaller platinum particle size on N-CNTs, which can significantly improve the performance and cycle durability compared to platinum on CNTs. Therefore, the support material selection is crucial in determining the behavior, performance, life and cost-effectiveness of whole fuel cells. Currently, carbon black (*e.g.* XC-72) with a high surface area is the commonly used catalyst support for both the anodes and cathodes in fuel-cell technology. However, aggregation of the catalytic metal nanoparticles resulting from weak interactions between the carbon-based electrochemical support materials and the catalytic noble metal nanoparticles could decrease the active surface area after long-term operation.[164] More importantly, both electrochemical carbon corrosion resulting from reaction with the HO^{2-} radical, which was formed as an intermediate oxygen reduction species, and dissolution of the active noble metal elements under normal operating conditions, were accelerated at high operation potentials. Some carbon materials (carbon nanotubes, carbon nanofibers, graphene and carbon nanocages) with a higher graphitic component exhibited desirable corrosion resistance.[165–171] Nevertheless, no matter how high the graphitic component in the carbon-based materials, carbon can still be oxidative under the operation conditions (high operation voltage and oxidative atmosphere at the cathode side) and this could become worse at the time of start-up or it could even turn off the fuel cell due to a much higher operation voltage (~1.4 V or higher).[129] Highly chemically stable conducting metal oxides, such as titania, tungsten oxide, alumina, niobia, ceria, silica, zirconia, and indium oxide, were developed as effective electrochemical supports for fuel cells; they can not only prevent carbon corrosion but can also introduce a synergistic co-catalytic effect between the noble metal and the conducting metal–oxide support.[10,151,152,172] Compared with carbon-based materials, the noble metal could be deposited more uniformly and with a smaller particle size on metal oxides due to the strong connection between the noble metal and conducting oxides. Our recent research clearly shows that the average particle size of platinum on a niobium-doped titanium oxide electrochemical support was much smaller than that on the surface of pure carbon nanotubes.[161]

Recently, niobium doped titanium oxides and tin oxides have been widely used as conductive metal oxide electrochemical supports due to their excellent electron conductivities (doping Nb^{5+} into TiO_2 or SnO_2 can donate electrons to the conduction band), excellent chemical stability and high corrosion resistance in various electrolytic media, including strong acid solution.[173–175] Stoichiometric Nb_2O_5 with a band gap of 3.4 eV is a pure insulator and electronic conductor, which could be essential after introducing Nb^{4+} ions and can be generated by creating oxygen deficiencies by heating Nb_2O_5 in a reducing atmosphere at high temperatures.[12] Another possible way is combining carbon black. Sasaki *et al.* firstly used niobia (Nb_2O_5 and NbO_2) as an electrochemical support for the ORR,[155] and Pt/NbO_2/C electrocatalysts with ultra-low platinum loading showed a superior ORR performance compared with a commercial Pt/C electrocatalyst. Platinum nanoparticles supported on carbon black, decorated with a niobium oxide phase, were also prepared for the ORR. It was found that hydrophilic Nb_xO_y-composite materials have lower intrinsic catalytic activity for oxygen reduction but offer better overall platinum mass utilization.[176] Therefore, the improved ORR performance after employing niobia as a support encourages us to investigate the mechanism of how the niobia affects the platinum, so that we can optimize the catalyst design. Electron density transfer from the d-orbitals of the metal to unoccupied p-orbitals of oxygen is commonly observed in metal–metal oxides, resulting in the formation of platinum–oxide. The reduced number of unoccupied p-orbitals of O at the metal–metal oxide interface could lead to weak Pt–O bonding, resulting in a fast oxygen reduction reaction. Zhang *et al.* showed that the binding energy of Pt–O has a strong dependence on the oxidation state of the support surface. Therefore, Pt on NbO exhibited a smoother surface than Pt on NbO_2 and Nb_2O_5 due to stronger binding of Pt at the NbO interface.[177] Therefore, Pt supported by NbO and

NbO_2 enhances the specific electrocatalytic activity compared with Pt on glassy carbon. Sasaki also thought that the superior mass activity of $Pt/NbO_2/C$ could be ascribed to the reduced OH adsorption, which was caused by lateral repulsion between PtOH and the oxide surface species.[155] However, the high temperature (generally 1000 °C) for the phase transformation of Nb_2O_5 to NbO_2 could lead to a larger particle size for NbO_2, which will limit the application of NbO_2 as an electrochemical support. Recently, a conducting NbO_2 phase was achieved at temperatures as low as 700 °C by firstly activating niobium oxide with a carbon coating.[16] Zhang *et al.* also used radio frequency magnetron sputtering to deposit NbO_2 on CNT arrays.[10] Fig. 16e shows images of NbO_2 on the CNT array. The CNTs were almost covered by NbO_2 (NbO_2/CNTs); after depositing Pt on the NbO_2/CNTs, almost no decrease in the electrochemical surface area and oxygen reduction reaction for the Pt/NbO_2/CNT catalyst was observed after as many as 10 000 cycles (Fig. 16c and d). However, a significant reduction in the ECSA (Fig. 16a) and the ORR (Fig. 16b) was observed for the Pt/CNT catalysts.

A one-dimensional niobium oxide electrochemical support also provides the benefits of a high surface area and easy gas diffusion in fuel cell technologies. Nanopillar and nanofiber niobium oxides were fabricated by glancing angle deposition (GLAD)[178] and electrospinning technologies,[179] respectively. After post-heat treatment at a high annealing temperature under a reductive atmosphere, the insulator, Nb_2O_5, could be converted into conductive NbO and NbO_2. An electrochemical performance test showed that the niobium–oxide supports could be stable under aggressive electrochemical testing (up to 1.4 V *vs.* RHE). As an electrochemical support, NbO_x and a nitrogen-doped graphene nanosheet composite with a sandwich-like structure has been designed for direct oxygen reduction reaction.[180] The enhanced ORR and high methanol tolerance could be attributed to the active oxygen vacancy in NbO_x and the synergistic coupling effect resulting from strong contact between NbO_x and the nitrogen-doped graphene nanosheets.

The poisoning of platinum active sites by strong absorption of a CO intermediate is another critical problem associated with the practical operation of fuel cells. This poisoning behavior will hinder further oxidation of methanol, resulting in a high onset potential at the anode side, which will significantly decrease the power densities of our fuel cells. The strong connection between platinum and metal oxide can not only change the energy level of d orbits in platinum, which could decrease the absorption of a CO intermediate on platinum active sites, but can also provide extra OH– functional groups in acid solution, which can be used to remove CO intermediates quickly so as to increase the kinetics of methanol oxidation. Therefore, many oxides, such as TiO_2, WO_3, ZrO_2, CeO_2, SnO_2 and Nb_2O_5, were used as effective electrochemical

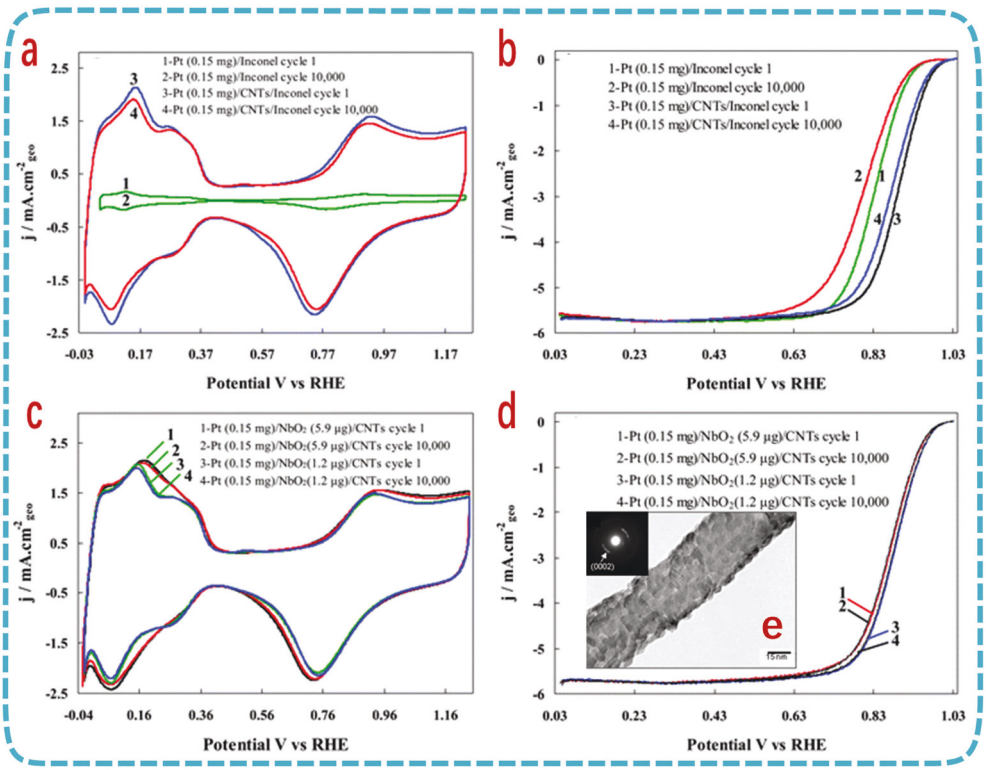

Fig. 16 CV and ORR curves of Pt/Inconel, Pt/CNT (a, b) and Pt/NbO_2/CNT (c, d) at cycle 1 and at cycle number 10 000. Conventional and high-resolution TEM micrographs of NbO_2 (1.2 mg)/CNT (e); adapted and reproduced, with permission, from ref. 10. Copyright 2012, Royal Society of Chemistry.

supporting materials in fuel cells.[151,152,161,164,181–183] Compared with other oxides, niobium-based oxides have the advantages of excellent chemical stability in acid conditions, high intrinsic catalytic activity and high oxygen storage capacity. Furthermore, niobium-based oxides exhibited an excellent synergistic effect in metal–metal oxide systems due to their well-known strong metal support interactions. Thus, it is expected that niobium-based oxides can provide mobile surface oxygen species to the noble metal surface by spillover effects to facilitate electro-oxidation of adsorbed CO or CO intermediates.[184–187] However, the low electronic conductivity of Nb_2O_5 also limits its application in methanol oxidation or formic acid oxidation. As with improving the electronic conductivities of Nb_2O_5 in LIBs and SCs, a general and effective method is introducing or combining it with carbon. Chun *et al.* investigated the effect of introducing Nb_2O_5 nanoparticles onto carbon-supported platinum to facilitate the electrochemical kinetics of CO and methanol oxidation.[188] Their results indicated that introducing niobium oxide into carbon-supported platinum can enhance the catalytic activity due to a bifunctional mechanism, in which Nb_2O_5 not only modified the electronic structure of platinum but also donated surface mobile oxygen by a spillover effect to Pt–CO absorbents, resulting in low oxidation potential. The electrochemical oxidation of ethanol is an 8-electron transfer reaction if the ethanol can be fully oxidized to carbon dioxide. Therefore, the splitting of the C–C bond in ethanol is crucial for the high activity of the electrochemical oxidation of ethanol. Pt-Nb_2O_5/carbon provided a more favorable environment for the ethanol oxidation process due to strong intrinsic metal–oxide interactions, which can provide an extra OH– group. However, this catalyst is still quite limited with respect to splitting the C–C bond. Recent research clearly showed that a larger Pt–NbO_x interfacial surface area in Nb_xRu_yO-supported Pt could be more effective with respect to splitting the C–C bond in acid electrolyte solution, although the kinetics of ethanol oxidation were relatively slower than for reference samples.[189,190] Actually, a unique catalytic behavior could be observed in the oxidation of CO and the dehydrogenation of much larger molecules when Pt nanoparticles were present on the reduced NbO_x subspecies. Pt and Pt–Pb-based nanoparticles supported by mesoporous highly crystalline niobium oxide–carbon composites were developed by a one-pot synthesis method,[11] as shown in Fig. 17. The dimensions, such as pore size and wall thickness, were controlled by simply varying the block-copolymer molecular weight or block weight fraction due to the structure-directing properties of the block-copolymer. The mesoporosity can prevent particle agglomeration and provide uniformly dispersed nanoparticles. A mesostructured material, CCM–NbO_2–C–Pt–Pb, which was prepared by this one-pot synthesis method, showed excellent electrochemical activity toward formic acid oxidation.

7. Outlook and future work

As a chemically stable, low-cost and environmentally friendly product, niobium-based oxides could be extensively used in LIBs, NIBs, SCs, VRBs and fuel cells, as summarized in Fig. 18. Their distinguished electrochemical performance (high capacitance for SCs, excellent cycle and rate performance for LIBs and NIBs) and high corrosion resistance under practical fuel-cell operation conditions could make them promising electrodes or electrochemical support materials for widespread industrial applications in batteries and fuel cell technologies. Their higher potential windows can prevent the formation of lithium dendrites and their specific lithium-ion-insertion behaviour keeps the crystal structure stable during charge–discharge processes, which makes them promising electrodes for LIBs. Compared with other transition-metal–oxide, Nb_2O_5 delivered a high capacitance and an excellent cycling performance because it can avoid agglomeration, thus increasing the

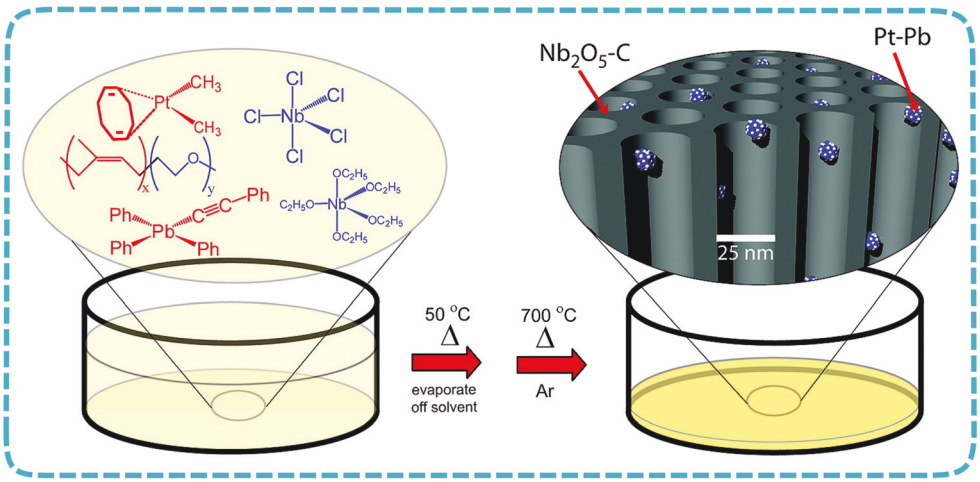

Fig. 17 Schematic representation of the demonstrated one-pot method. Adapted and reproduced, with permission, from ref. 11. Copyright 2009, American Chemical Society.

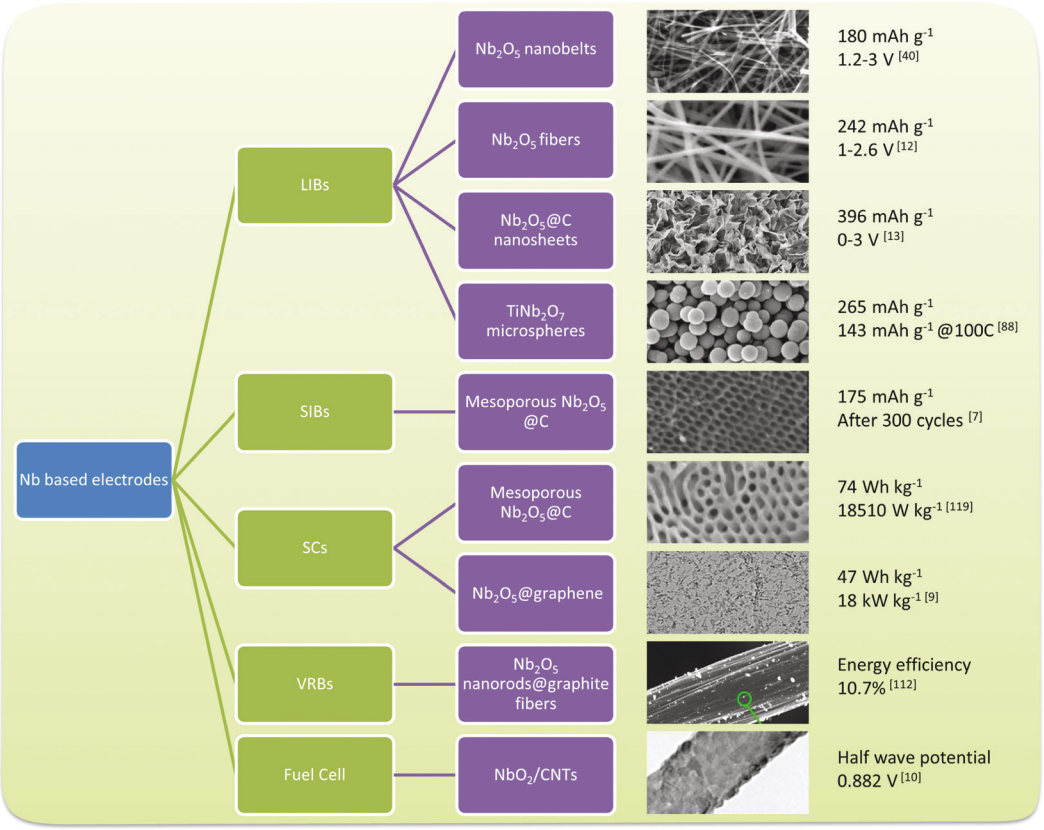

Fig. 18 Summary of the applications of niobium-based oxides.

surface area exposed to electrolyte. Meanwhile, the wide potential window for Nb_2O_5 as a supercapacitor results in a high energy density. The unique chemical stability and conductivity of modified niobium oxides under acid conditions (most transition metal oxides are not stable under acid conditions) would provide an effective and promising way to solve the dilemma of degradation under practical operating conditions in fuel cells. However, the low ion and electron conductivities, low surface area (resulting from a high annealing temperature) and relatively high-temperature synthesis methods still pose significant challenges for practical industry application. On the other hand, these disadvantages also give us directions for future work.

(1) A facile, low cost and environmentally friendly synthetic approach is necessary for realizing the large-scale production of niobium-based oxide nanostructures.

(2) Developing a new material design to make full utilization of the electrode materials can achieve the ultimate goals of high energy and power densities.

(3) A unique architecture for a 3D current collector can facilitate easy penetration of the electrolyte solution into the electrode, which can ensure that the ions are accessible to regions far beyond the surface.

(4) There is still a need to fully understand the relationship between niobium-based oxide nanostructures and their electrochemical behaviour (*e.g.* the kinetics of charge transfer and ion diffusion at the electrode/electrolyte interface), which can assist future optimization of the synthesis parameters and material properties.

(5) Since platinum nanoparticles could not be easily deposited on a smaller electrochemical support, 0D conducting oxides with a smaller particle size could not meet the requirements for the electrochemical support although they could have a high surface area; therefore, preparing highly conductive and high-surface-area niobium-based oxides with 1D or 2D structures (*e.g.* nanosheets, nanotubes or nanorods) could be a possible solution towards an effective electrochemical support in fuel cell technologies.

Acknowledgements

G. C. greatly thanks the 2015 ECS Edward G. Weston Summer Fellowship and Chinese Government Award for Outstanding Self-Financed Students Abroad from China Scholarship Council. G. Z. acknowledges the support from 973 Program Special Funds for the Chief Young Scientist (2015CB358600), the Excellent Young Scholar Fund from the National Natural Science Foundation of China (21422103), the Jiangsu Fund for Distinguished Young Scientist (BK20140010), and the Priority Academic Program Development of Jiangsu Higher Education Institutions (PAPD). H. L. acknowledges the partial funding

support from the National Science Foundation DMR-1449035, the New Mexico EPSCoR with NSF-1301346, and Argonne National Laboratory. Argonne, a U.S. Department of Energy Office of Science laboratory, is operated under Contract no. DE-AC02-06CH11357.

References

1 M. Armand and J. M. Tarascon, *Nature*, 2008, **451**, 652–657.
2 P. G. Bruce, B. Scrosati and J. M. Tarascon, *Angew. Chem., Int. Ed.*, 2008, **47**, 2930–2946.
3 C. Liu, F. Li, L.-P. Ma and H.-M. Cheng, *Adv. Mater.*, 2010, **22**, E28–E62.
4 Z. Chen, D. Higgins, A. Yu, L. Zhang and J. Zhang, *Energy Environ. Sci.*, 2011, **4**, 3167–3192.
5 N. V. Long, Y. Yang, C. Minh Thi, N. V. Minh, Y. Cao and M. Nogami, *Nano Energy*, 2013, **2**, 636–676.
6 Z.-F. Li, L. Xin, F. Yang, Y. Liu, Y. Liu, H. Zhang, L. Stanciu and J. Xie, *Nano Energy*, 2015, **16**, 281–292.
7 H. Kim, E. Lim, C. Jo, G. Yoon, J. Hwang, S. Jeong, J. Lee and K. Kang, *Nano Energy*, 2015, **16**, 62–70.
8 X. Wang, C. Yan, J. Yan, A. Sumboja and P. S. Lee, *Nano Energy*, 2015, **11**, 765–772.
9 L. Kong, C. Zhang, J. Wang, W. Qiao, L. Ling and D. Long, *ACS Nano*, 2015, **9**, 11200–11208.
10 L. Zhang, L. Wang, C. M. B. Holt, B. Zahiri, Z. Li, K. Malek, T. Navessin, M. H. Eikerling and D. Mitlin, *Energy Environ. Sci.*, 2012, **5**, 6156–6172.
11 M. C. Orilall, F. Matsumoto, Q. Zhou, H. Sai, H. D. Abruña, F. J. DiSalvo and U. Wiesner, *J. Am. Chem. Soc.*, 2009, **131**, 9389–9395.
12 A. L. Viet, M. V. Reddy, R. Jose, B. V. R. Chowdari and S. Ramakrishna, *J. Phys. Chem. C*, 2010, **114**, 664–671.
13 L. Wang, B. Y. Ruan, J. T. Xu, H. K. Liu and J. M. Ma, *RSC Adv.*, 2015, **5**, 36104–36107.
14 J. E. Yoo, J. Park, G. Cha and J. Choi, *Thin Solid Films*, 2013, **531**, 583–587.
15 X. Wang, G. Li, Z. Chen, V. Augustyn, X. Ma, G. Wang, B. Dunn and Y. Lu, *Adv. Energy Mater.*, 2011, **1**, 1089–1093.
16 K. Huang, Y. Li, L. Yan and Y. Xing, *RSC Adv.*, 2014, **4**, 9701–9708.
17 Y. Cai, X. Li, L. Wang, H. Y. Gao, Y. N. Zhao and J. M. Ma, *J. Mater. Chem. A*, 2015, **3**, 1396–1399.
18 X. Chia, A. Y. S. Eng, A. Ambrosi, S. M. Tan and M. Pumera, *Chem. Rev.*, 2015, **115**, 11941–11966.
19 Z. Yang, D. Choi, S. Kerisit, K. M. Rosso, D. Wang, J. Zhang, G. Graff and J. Liu, *J. Power Sources*, 2009, **192**, 588–598.
20 A. S. Arico, P. Bruce, B. Scrosati, J. M. Tarascon and W. Van Schalkwijk, *Nat. Mater.*, 2005, **4**, 366–377.
21 X. H. Rui, Q. Y. Yan, M. Skyllas-Kazacos and T. M. Lim, *J. Power Sources*, 2014, **258**, 19–38.
22 F. Y. Cheng, J. Liang, Z. L. Tao and J. Chen, *Adv. Mater.*, 2011, **23**, 1695–1715.
23 S. F. Lou, X. Q. Cheng, Y. L. Ma, C. Y. Du, Y. Z. Gao and G. P. Yin, *Prog. Chem.*, 2015, **27**, 297–309.
24 V. Aravindan, Y. S. Lee and S. Madhavi, *Adv. Energy Mater.*, 2015, **5**, 1402225.
25 T. F. Yi, S. Y. Yang and Y. Xie, *J. Mater. Chem. A*, 2015, **3**, 5750–5777.
26 K. Tanabe and S. Okazaki, *Appl. Catal., A*, 1995, **133**, 191–218.
27 G. Barkhordarian, T. Klassen and R. Bormann, *Scr. Mater.*, 2003, **49**, 213–217.
28 I. Nowak and M. Ziolek, *Chem. Rev.*, 1999, **99**, 3603–3624.
29 X. S. Fang, L. F. Hu, K. F. Huo, B. Gao, L. J. Zhao, M. Y. Liao, P. K. Chu, Y. Bando and D. Golberg, *Adv. Funct. Mater.*, 2011, **21**, 3907–3915.
30 N. Kumagai, Y. Tateshita, Y. Takatsuka, M. Baba, T. Ikeda and K. Tanno, *J. Power Sources*, 1995, **54**, 175–179.
31 R. A. Rani, A. S. Zoolfakar, A. P. O'Mullane, M. W. Austin and K. Kalantar-Zadeh, *J. Mater. Chem. A*, 2014, **2**, 15683–15703.
32 H. Schäfer, R. Gruehn and F. Schulte, *Angew. Chem., Int. Ed. Engl.*, 1966, **5**, 40–52.
33 Y. Zhao, X. Zhou, L. Ye and S. C. E. Tsang, *Nano Rev.*, 2012, **3**, 17631.
34 N. Kumagai, K. Tanno, T. Nakajima and N. Watanabe, *Electrochim. Acta*, 1983, **28**, 17–22.
35 N. Kumagai, Y. Koishikawa, S. Komaba and N. Koshiba, *J. Electrochem. Soc.*, 1999, **146**, 3203–3210.
36 R. Kodama, Y. Terada, I. Nakai, S. Komaba and N. Kumagai, *J. Electrochem. Soc.*, 2006, **153**, A583–A588.
37 X. H. Rui, H. T. Tan and Q. Y. Yan, *Nanoscale*, 2014, **6**, 9889–9924.
38 H. T. Tan, X. H. Rui, W. P. Sun, Q. Y. Yan and T. M. Lim, *Nanoscale*, 2015, **7**, 14595–14607.
39 M. V. Reddy, R. Jose, A. Le Viet, K. I. Ozoemena, B. V. R. Chowdari and S. Ramakrishna, *Electrochim. Acta*, 2014, **128**, 198–202.
40 M. D. Wei, K. Wei, M. Ichihara and H. Zhou, *Electrochem. Commun.*, 2008, **10**, 980–983.
41 H. Zhang, Y. Wang, P. Liu, S. L. Chou, J. Z. Wang, H. Liu, G. Wang and H. Zhao, *ACS Nano*, 2016, **10**, 507–514.
42 L. Kong, C. Zhang, S. Zhang, J. Wang, R. Cai, C. Lv, W. Qiao, L. Ling and D. Long, *J. Mater. Chem. A*, 2014, **2**, 17962–17970.
43 G. Chen, E. Fu, M. Zhou, Y. Xu, L. Fei, S. Deng, V. Chaitanya, Y. Wang and H. Luo, *J. Alloys Compd.*, 2013, **578**, 349–354.
44 X. H. Rui, X. X. Zhao, Z. Y. Lu, H. T. Tan, D. H. Sim, H. H. Hng, R. Yazami, T. M. Lim and Q. Y. Yan, *ACS Nano*, 2013, **7**, 5637–5646.
45 M. Liu, C. Yan and Y. Zhang, *Sci. Rep.*, 2015, **5**, 8326.
46 H. Y. Luo, M. D. Wei and K. M. Wei, *Mater. Chem. Phys.*, 2010, **120**, 6–9.
47 Y. X. Tang, X. H. Rui, Y. Y. Zhang, T. M. Lim, Z. L. Dong, H. H. Hng, X. D. Chen, Q. Y. Yan and Z. Chen, *J. Mater. Chem. A*, 2013, **1**, 82–88.

48 X. H. Rui, H. T. Tan, D. H. Sim, W. L. Liu, C. Xu, H. H. Hng, R. Yazami, T. M. Lim and Q. Y. Yan, *J. Power Sources*, 2013, **222**, 97–102.
49 R. Liu, J. Duay and S. B. Lee, *Chem. Commun.*, 2011, **47**, 1384–1404.
50 M. Sasidharan, N. Gunawardhana, M. Yoshio and K. Nakashima, *Mater. Res. Bull.*, 2012, **47**, 2161–2164.
51 S. Q. Guo, X. Zhang, Z. Zhou, G. D. Gao and L. Liu, *J. Mater. Chem. A*, 2014, **2**, 9236–9243.
52 M. M. Rahman, R. A. Rani, A. Z. Sadek, A. S. Zoolfakar, M. R. Field, T. Ramireddy, K. Kalantar-zadeh and Y. Chen, *J. Mater. Chem. A*, 2013, **1**, 11019–11025.
53 S. H. Kang, C. M. Park, J. Lee and J. H. Kim, *J. Electroanal. Chem.*, 2015, **746**, 45–50.
54 H. Wen, Z. F. Liu, J. Wang, Q. B. Yang, Y. X. Li and J. Yu, *Appl. Surf. Sci.*, 2011, **257**, 10084–10088.
55 P. Arunkumar, A. G. Ashish, B. Babu, S. Sarang, A. Suresh, C. H. Sharma, M. Thalakulam and M. M. Shaijumon, *RSC Adv.*, 2015, **5**, 59997–60004.
56 P. Arunkumar, A. G. Ashish, B. Babu, S. Sarang, A. Suresh, C. H. Sharma, M. Thalakulam and M. M. Shaijumon, *RSC Adv.*, 2015, **5**, 59997–60004.
57 G. Li, X. L. Wang and X. M. Ma, *J. Energy Chem.*, 2013, **22**, 357–362.
58 L. Yan, Y. Xu, M. Zhou, G. Chen, S. Deng, S. Smirnov, H. Luo and G. Zou, *Electrochim. Acta*, 2015, **169**, 73–81.
59 N. Kumagai, S. Komaba and N. Kumagai, *MRS Proc.*, 1999, **575**, 39–48.
60 L. Yan, G. Chen, M. Zhou and H. Luo, *ECS Trans.*, 2015, **66**, 277–283.
61 Y. Li, C. W. Sun and J. B. Goodenough, *Chem. Mater.*, 2011, **23**, 2292–2294.
62 J. T. Son, *Electrochem. Commun.*, 2004, **6**, 990–994.
63 Q. Fan, L. Lei and Y. Sun, *Nanoscale*, 2014, **6**, 7188–7192.
64 Q. Fan, L. Lei, G. Yin and Y. Sun, *Chem. Commun.*, 2014, **50**, 2370–2373.
65 V. Pralong, M. A. Reddy, V. Caignaert, S. Malo, O. I. Lebedev, U. V. Varadaraju and B. Raveau, *Chem. Mater.*, 2011, **23**, 1915–1922.
66 Z. Jian, X. Lu, Z. Fang, Y.-S. Hu, J. Zhou, W. Chen and L. Chen, *Electrochem. Commun.*, 2011, **13**, 1127–1130.
67 J. E. Kwak, H. Yun and H. K. Chae, *Acta Crystallogr., Sect. E: Struct. Rep. Online*, 2005, **61**, I132–I134.
68 J.-T. Han, D.-Q. Liu, S.-H. Song, Y. Kim and J. B. Goodenough, *Chem. Mater.*, 2009, **21**, 4753–4755.
69 Y. Lu, J. B. Goodenough, G. K. P. Dathar, G. Henkelman, J. Wu and K. Stevenson, *Chem. Mater.*, 2011, **23**, 3210–3216.
70 Q. X. Fu and F. Tietz, *Fuel Cells*, 2008, **8**, 283–293.
71 J. T. Han, Y. H. Huang and J. B. Goodenough, *Chem. Mater.*, 2011, **23**, 2027–2029.
72 X. Y. Wu, J. Miao, W. Z. Han, Y. S. Hu, D. F. Chen, J. S. Lee, J. Kim and L. Q. Chen, *Electrochem. Commun.*, 2012, **25**, 39–42.
73 J. F. Colin, V. Pralong, M. Hervieu, V. Caignaert and B. Raveau, *Chem. Mater.*, 2008, **20**, 1534–1540.
74 R. J. Cava, D. W. Murphy and S. M. Zahurak, *J. Electrochem. Soc.*, 1983, **130**, 2345–2351.
75 X. Lu, Z. Jian, Z. Fang, L. Gu, Y.-S. Hu, W. Chen, Z. Wang and L. Chen, *Energy Environ. Sci.*, 2011, **4**, 2638–2644.
76 J.-T. Han and J. B. Goodenough, *Chem. Mater.*, 2011, **23**, 3404–3407.
77 L. Fei, Y. Xu, X. Wu, Y. Li, P. Xie, S. Deng, S. Smirnov and H. Luo, *Nanoscale*, 2013, **5**, 11102–11107.
78 C. Jo, Y. Kim, J. Hwang, J. Shim, J. Chun and J. Lee, *Chem. Mater.*, 2014, **26**, 3508–3514.
79 B. Guo, X. Yu, X.-G. Sun, M. Chi, Z.-A. Qiao, J. Liu, Y.-S. Hu, X.-Q. Yang, J. B. Goodenough and S. Dai, *Energy Environ. Sci.*, 2014, **7**, 2220–2226.
80 Q. Cheng, J. Liang, N. Lin, C. Guo, Y. Zhu and Y. Qian, *Electrochim. Acta*, 2015, **176**, 456–462.
81 H. Li, L. Shen, G. Pang, S. Fang, H. Luo, K. Yang and X. Zhang, *Nanoscale*, 2015, **7**, 619–624.
82 K. Tang, X. Mu, P. A. van Aken, Y. Yu and J. Maier, *Adv. Energy Mater.*, 2013, **3**, 49–53.
83 S. Jayaraman, V. Aravindan, P. Suresh Kumar, W. Chui Ling, S. Ramakrishna and S. Madhavi, *ACS Appl. Mater. Interfaces*, 2014, **6**, 8660–8666.
84 S. Lou, Y. Ma, X. Cheng, J. Gao, Y. Gao, P. Zuo, C. Du and G. Yin, *Chem. Commun.*, 2015, **51**, 17293.
85 C. Lin, S. Yu, S. Wu, S. Lin, Z.-Z. Zhu, J. Li and L. Lu, *J. Mater. Chem. A*, 2015, **3**, 8627–8635.
86 A. G. Ashish, P. Arunkumar, B. Babu, P. Manikandan, S. Sarang and M. M. Shaijumon, *Electrochim. Acta*, 2015, **176**, 285–292.
87 H. Park, T. Song and U. Paik, *J. Mater. Chem. A*, 2015, **3**, 8590–8596.
88 H. Park, H. B. Wu, T. Song, X. W. Lou and U. Paik, *Adv. Energy Mater.*, 2015, **5**, 1401945–1401951.
89 T. Takashima, T. Tojo, R. Inada and Y. Sakurai, *J. Power Sources*, 2015, **276**, 113–119.
90 W. L. Wang, B.-Y. Oh, J.-Y. Park, H. Ki, J. Jang, G.-Y. Lee, H.-B. Gu and M.-H. Ham, *J. Power Sources*, 2015, **300**, 272–278.
91 X. Wu, J. Miao, W. Han, Y.-S. Hu, D. Chen, J.-S. Lee, J. Kim and L. Chen, *Electrochem. Commun.*, 2012, **25**, 39–42.
92 Q. Cheng, J. Liang, Y. Zhu, L. Si, C. Guo and Y. Qian, *J. Mater. Chem. A*, 2014, **2**, 17258–17262.
93 C. Lin, G. Wang, S. Lin, J. Li and L. Lu, *Chem. Commun.*, 2015, **51**, 8970–8973.
94 G. Li, X. Wang, Z. Chen, X. Ma and Y. Lu, *Electrochim. Acta*, 2013, **102**, 351–357.
95 G. Li, X. Wang and X. Ma, *J. Mater. Chem. A*, 2013, **1**, 12409–12412.
96 B. Zachau-Christiansen, K. West, T. Jacobsen and S. Skaarup, *Solid State Ionics*, 1992, **53**, 364–369.
97 M. A. Reddy and U. V. Varadaraju, *Chem. Mater.*, 2008, **20**, 4557–4559.
98 H. Yamada, M. Hibino and T. Kudo, *Solid State Ionics*, 2001, **140**, 249–255.
99 A. F. Fuentes, A. Martinez De La Cruz and L. M. Torres-Martinez, *Solid State Ionics*, 1996, **92**, 103–111.

100 D. Saritha, V. Pralong, U. V. Varadaraju and B. Raveau, *J. Solid State Chem.*, 2010, **183**, 988–993.
101 X. Li, H. Zhang, Z. Mai, H. Zhang and I. Vankelecom, *Energy Environ. Sci.*, 2011, **4**, 1147–1160.
102 A. Parasuraman, T. M. Lim, C. Menictas and M. Skyllas-Kazacos, *Electrochim. Acta*, 2013, **101**, 27–40.
103 X. Rui, A. Parasuraman, W. Liu, D. H. Sim, H. H. Hng, Q. Yan, T. M. Lim and M. Skyllas-Kazacos, *Carbon*, 2013, **64**, 464–471.
104 B. Schwenzer, J. Zhang, S. Kim, L. Li, J. Liu and Z. Yang, *ChemSusChem*, 2011, **4**, 1388–1406.
105 S. Wang, X. Zhao, T. Cochell and A. Manthiram, *J. Phys. Chem. Lett.*, 2012, **3**, 2164–2167.
106 J. Jin, X. Fu, Q. Liu, Y. Liu, Z. Wei, K. Niu and J. Zhang, *ACS Nano*, 2013, **7**, 4764–4773.
107 X. Rui, M. O. Oo, D. H. Sim, S. C. Raghu, Q. Yan, T. M. Lim and M. Skyllas-Kazacos, *Electrochim. Acta*, 2012, **85**, 175–181.
108 T.-M. Tseng, R.-H. Huang, C.-Y. Huang, K.-L. Hsueh and F.-S. Shieu, *J. Electrochem. Soc.*, 2013, **160**, A690–A696.
109 M. Park, J. Ryu and J. Cho, *Chem. – Asian J.*, 2015, **10**, 2096–2110.
110 L. P. Wang, L. Yu, R. Satish, J. Zhu, Q. Yan, M. Srinivasan and Z. Xu, *RSC Adv.*, 2014, **4**, 37389–37394.
111 C. Yao, H. Zhang, T. Liu, X. Li and Z. Liu, *J. Power Sources*, 2012, **218**, 455–461.
112 B. Li, M. Gu, Z. Nie, X. Wei, C. Wang, V. Sprenkle and W. Wang, *Nano Lett.*, 2014, **14**, 158–165.
113 L. Li, S. Kim, W. Wang, M. Vijayakumar, Z. Nie, B. Chen, J. Zhang, G. Xia, J. Hu, G. Graff, J. Liu and Z. Yang, *Adv. Energy Mater.*, 2011, **1**, 394–400.
114 M. R. Arcila-Velez, J. Zhu, A. Childress, M. Karakaya, R. Podila, A. M. Rao and M. E. Roberts, *Nano Energy*, 2014, **8**, 9–16.
115 J. Chen, J. Xu, S. Zhou, N. Zhao and C.-P. Wong, *Nano Energy*, 2015, **15**, 719–728.
116 J. P. Zheng, P. J. Cygan and T. R. Jow, *J. Electrochem. Soc.*, 1995, **142**, 2699–2703.
117 V. Augustyn, J. Come, M. A. Lowe, J. W. Kim, P.-L. Taberna, S. H. Tolbert, H. D. Abruña, P. Simon and B. Dunn, *Nat. Mater.*, 2013, **12**, 518–522.
118 A. A. Lubimtsev, P. R. C. Kent, B. G. Sumpter and P. Ganesh, *J. Mater. Chem. A*, 2013, **1**, 14951–14956.
119 E. Lim, H. Kim, C. Jo, J. Chun, K. Ku, S. Kim, H. I. Lee, I.-S. Nam, S. Yoon, K. Kang and J. Lee, *ACS Nano*, 2014, **8**, 8968–8978.
120 E. Lim, C. Jo, H. Kim, M.-H. Kim, Y. Mun, J. Chun, Y. Ye, J. Hwang, K.-S. Ha, K. C. Roh, K. Kang, S. Yoon and J. Lee, *ACS Nano*, 2015, **9**, 7497–7505.
121 X. Wang, G. Li, R. Tjandra, X. Fan, X. Xiao and A. Yu, *RSC Adv.*, 2015, **5**, 41179–41185.
122 C. Zhang, R. Maloney, M. R. Lukatskaya, M. Beidaghi, B. Dyatkin, E. Perre, D. Long, W. Qiao, B. Dunn and Y. Gogotsi, *J. Power Sources*, 2015, **274**, 121–129.
123 M. Rose, E. Kockrick, I. Senkovska and S. Kaskel, *Carbon*, 2010, **48**, 403–407.
124 L. Kong, C. Zhang, J. Wang, D. Long, W. Qiao and L. Ling, *Mater. Chem. Phys.*, 2015, **149–150**, 495–504.
125 H. Li, L. Shen, J. Wang, S. Fang, Y. Zhang, H. Dou and X. Zhang, *J. Mater. Chem. A*, 2015, **3**, 16785–16790.
126 X. Wang and G. Shen, *Nano Energy*, 2015, **15**, 104–115.
127 X. Wang and P. S. Lee, *J. Mater. Chem. A*, 2015, **3**, 21706–21712.
128 V. Aravindan, J. Sundaramurthy, A. Jain, P. S. Kumar, W. C. Ling, S. Ramakrishna, M. P. Srinivasan and S. Madhavi, *ChemSusChem*, 2014, **7**, 1858–1863.
129 S. Sharma and B. G. Pollet, *J. Power Sources*, 2012, **208**, 96–119.
130 N. Rajalakshmi, N. Lakshmi and K. S. Dhathathreyan, *Int. J. Hydrogen Energy*, 2008, **33**, 7521–7526.
131 K. S. Howe and K. Kendall, *J. Fuel Cell Sci. Technol.*, 2011, **8**, 034502–034502.
132 L. Yan, H. Ding, Z. Zhu and X. Xue, *J. Power Sources*, 2011, **196**, 9352–9355.
133 W. Sun, L. Yan, B. Lin, S. Zhang and W. Liu, *J. Power Sources*, 2010, **195**, 3155–3158.
134 A. H. C. Sirk, J. M. Hill, S. K. Y. Kung and V. I. Birss, *J. Phys. Chem. B*, 2004, **108**, 689–695.
135 Y. Chen, Y. Lin, Y. Zhang, S. Wang, D. Su, Z. Yang, M. Han and F. Chen, *Nano Energy*, 2014, **8**, 25–33.
136 A. Serov, K. Artyushkova, E. Niangar, C. Wang, N. Dale, F. Jaouen, M.-T. Sougrati, Q. Jia, S. Mukerjee and P. Atanassov, *Nano Energy*, 2015, **16**, 293–300.
137 C. Yang, J. Li, Y. Lin, J. Liu, F. Chen and M. Liu, *Nano Energy*, 2015, **11**, 704–710.
138 L. Feng, K. Li, J. Chang, C. Liu and W. Xing, *Nano Energy*, 2015, **15**, 462–469.
139 K. A. Kuttiyiel, Y. Choi, S.-M. Hwang, G.-G. Park, T.-H. Yang, D. Su, K. Sasaki, P. Liu and R. R. Adzic, *Nano Energy*, 2015, **13**, 442–449.
140 K. Elbert, J. Hu, Z. Ma, Y. Zhang, G. Chen, W. An, P. Liu, H. S. Isaacs, R. R. Adzic and J. X. Wang, *ACS Catal.*, 2015, **5**, 6764–6772.
141 S. Guo, S. Dong and E. Wang, *ACS Nano*, 2010, **4**, 547–555.
142 S. Guo, S. Zhang and S. Sun, *Angew. Chem., Int. Ed.*, 2013, **52**, 8526–8544.
143 S. Guo, S. Zhang, L. Wu and S. Sun, *Angew. Chem., Int. Ed.*, 2012, **124**, 11940–11943.
144 H. Zhu, S. Zhang, S. Guo, D. Su and S. Sun, *J. Am. Chem. Soc.*, 2013, **135**, 7130–7133.
145 S. Guo, D. Li, H. Zhu, S. Zhang, N. M. Markovic, V. R. Stamenkovic and S. Sun, *Angew. Chem., Int. Ed.*, 2013, **52**, 3465–3468.
146 S. Guo, S. Dong and E. Wang, *J. Phys. Chem. C*, 2008, **112**, 2389–2393.
147 Y.-J. Wang, N. Zhao, B. Fang, H. Li, X. T. Bi and H. Wang, *Chem. Rev.*, 2015, **115**, 3433–3467.
148 S. Chao, Q. Cui, K. Wang, Z. Bai, L. Yang and J. Qiao, *J. Power Sources*, 2015, **288**, 128–135.
149 M. Xiao, J. Zhu, L. Feng, C. Liu and W. Xing, *Adv. Mater.*, 2015, **27**, 2521–2527.

150 J. Liang, Y. Jiao, M. Jaroniec and S. Z. Qiao, *Angew. Chem., Int. Ed.*, 2012, **51**, 11496–11500.
151 V. T. T. Ho, C.-J. Pan, J. Rick, W.-N. Su and B.-J. Hwang, *J. Am. Chem. Soc.*, 2011, **133**, 11716–11724.
152 D. Wang, C. V. Subban, H. Wang, E. Rus, F. J. DiSalvo and H. D. Abruña, *J. Am. Chem. Soc.*, 2010, **132**, 10218–10220.
153 J. L. Fernández, V. Raghuveer, A. Manthiram and A. J. Bard, *J. Am. Chem. Soc.*, 2005, **127**, 13100–13101.
154 D. Geng, Y. Chen, Y. Chen, Y. Li, R. Li, X. Sun, S. Ye and S. Knights, *Energy Environ. Sci.*, 2011, **4**, 760–764.
155 K. Sasaki, L. Zhang and R. R. Adzic, *Phys. Chem. Chem. Phys.*, 2008, **10**, 159–167.
156 A. Serov and C. Kwak, *Appl. Catal., B*, 2009, **90**, 313–320.
157 A. Chandan, M. Hattenberger, A. El-kharouf, S. Du, A. Dhir, V. Self, B. G. Pollet, A. Ingram and W. Bujalski, *J. Power Sources*, 2013, **231**, 264–278.
158 C. Zhu, S. Guo and S. Dong, *J. Mater. Chem.*, 2012, **22**, 14851–14855.
159 J. Kua and W. A. Goddard, *J. Am. Chem. Soc.*, 1999, **121**, 10928–10941.
160 E. J. Coleman, M. H. Chowdhury and A. C. Co, *ACS Catal.*, 2015, **5**, 1245–1253.
161 L. Yan, K. Huang, Y. Chen and Y. Xing, *ECS Electrochem. Lett.*, 2014, **3**, F27–F29.
162 Y. Chen, J. Wang, H. Liu, R. Li, X. Sun, S. Ye and S. Knights, *Electrochem. Commun.*, 2009, **11**, 2071–2076.
163 Y. Chen, J. Wang, H. Liu, M. N. Banis, R. Li, X. Sun, T.-K. Sham, S. Ye and S. Knights, *J. Phys. Chem. C*, 2011, **115**, 3769–3776.
164 K. Huang, K. Sasaki, R. R. Adzic and Y. Xing, *J. Mater. Chem.*, 2012, **22**, 16824–16832.
165 K. Gong, F. Du, Z. Xia, M. Durstock and L. Dai, *Science*, 2009, **323**, 760–764.
166 Y. Li, W. Zhou, H. Wang, L. Xie, Y. Liang, F. Wei, J.-C. Idrobo, S. J. Pennycook and H. Dai, *Nat. Nanotechnol.*, 2012, **7**, 394–400.
167 Y.-H. Qin, Y.-B. Jia, Y. Jiang, D.-F. Niu, X.-S. Zhang, X.-G. Zhou, L. Niu and W.-K. Yuan, *Int. J. Hydrogen Energy*, 2012, **37**, 7373–7377.
168 Y.-H. Qin, Y. Jiang, D.-F. Niu, X.-S. Zhang, X.-G. Zhou, L. Niu and W.-K. Yuan, *J. Power Sources*, 2012, **215**, 130–134.
169 Y.-H. Qin, H.-H. Yang, X.-S. Zhang, P. Li and C.-A. Ma, *Int. J. Hydrogen Energy*, 2010, **35**, 7667–7674.
170 Y.-H. Qin, H.-H. Yang, X.-S. Zhang, P. Li, X.-G. Zhou, L. Niu and W.-K. Yuan, *Carbon*, 2010, **48**, 3323–3329.
171 Y.-H. Qin, J. Yue, H.-H. Yang, X.-S. Zhang, X.-G. Zhou, L. Niu and W.-K. Yuan, *J. Power Sources*, 2011, **196**, 4609–4612.
172 Z. Zhang, J. Liu, J. Gu, L. Su and L. Cheng, *Energy Environ. Sci.*, 2014, **7**, 2535–2558.
173 Q. Du, J. Wu and H. Yang, *ACS Catal.*, 2014, **4**, 144–151.
174 Y.-J. Wang, D. P. Wilkinson and J. Zhang, *Dalton Trans.*, 2012, **41**, 1187–1194.
175 T. Tsukatsune, Y. Takabatake, Z. Noda, T. Daio, A. Zaitsu, S. M. Lyth, A. Hayashi and K. Sasaki, *J. Electrochem. Soc.*, 2014, **161**, F1208–F1213.
176 B. B. Blizanac, S. Pylypenko, T. S. Olson, D. Konopka and P. Atanassov, *J. Electrochem. Soc.*, 2011, **158**, B485–B491.
177 L. Zhang, L. Wang, C. M. B. Holt, T. Navessin, K. Malek, M. H. Eikerling and D. Mitlin, *J. Phys. Chem. C*, 2010, **114**, 16463–16474.
178 A. Bonakdarpour, R. T. Tucker, M. D. Fleischauer, N. A. Beckers, M. J. Brett and D. P. Wilkinson, *Electrochim. Acta*, 2012, **85**, 492–500.
179 K. Senevirathne, R. Hui, S. Campbell, S. Ye and J. Zhang, *Electrochim. Acta*, 2012, **59**, 538–547.
180 Q. Wu, L. Liao, Q. Zhang, Y. Nie, J. Xiao, S. Wang, S. Dai, Q. Gao, Y. Zhang, X. Sun, B. Liu and Y. Tang, *Electrochim. Acta*, 2015, **158**, 42–48.
181 K. Huang, Y. Li and Y. Xing, *J. Mater. Res.*, 2013, **28**, 454–460.
182 Y.-H. Qin, H.-H. Yang, R.-L. Lv, W.-G. Wang and C.-W. Wang, *Electrochim. Acta*, 2013, **106**, 372–377.
183 Y.-H. Qin, Y. Zhuang, R.-L. Lv, T.-L. Wang, W.-G. Wang and C.-W. Wang, *Electrochim. Acta*, 2015, **154**, 77–82.
184 P. Justin, P. Hari Krishna Charan and G. Ranga Rao, *Appl. Catal., B*, 2010, **100**, 510–515.
185 T. Rocha, F. Ibanhi, F. Colmati, J. Linares, V. Paganin and E. Gonzalez, *J. Appl. Electrochem.*, 2013, **43**, 817–827.
186 K. Sasaki and R. R. Adzic, *J. Electrochem. Soc.*, 2008, **155**, B180–B186.
187 N. Zhang, S. Zhang, Y. Gao and G. Yin, *Fuel Cells*, 2013, **13**, 895–902.
188 H.-J. Chun, D. B. Kim, D.-H. Lim, W.-D. Lee and H.-I. Lee, *Int. J. Hydrogen Energy*, 2010, **35**, 6399–6408.
189 D. A. Konopka, M. Li, K. Artyushkova, N. Marinkovic, K. Sasaki, R. Adzic, T. L. Ward and P. Atanassov, *J. Phys. Chem. C*, 2011, **115**, 3043–3056.
190 D. A. Konopka, S. Pylypenko, P. Atanassov and T. L. Ward, *ACS Appl. Mater. Interfaces*, 2010, **2**, 86–95.